



# Side-lobe Can Know More: Towards Simultaneous Communication and Sensing for mmWave

QIAN YANG, Southern University of Science and Technology, China and Peng Cheng Laboratory, China

HENGXIN WU, Southern University of Science and Technology, China

QIANYI HUANG, Sun Yat-sen University, China and Peng Cheng Laboratory, China

JIN ZHANG, Southern University of Science and Technology, China and Peng Cheng Laboratory, China

HAO CHEN, Peng Cheng Laboratory, China

WEICHAO LI, Peng Cheng Laboratory, China

XIAOFENG TAO, Beijing University of Posts and Telecommunications, China and Peng Cheng Laboratory, China

QIAN ZHANG, Hong Kong University of Science and Technology, China

Thanks to the wide bandwidth, large antenna array, and short wavelength, millimeter wave (mmWave) has superior performance in both communication and sensing. Thus, the integration of sensing and communication is a developing trend for the mmWave band. However, the directional transmission characteristics of the mmWave limits the sensing scope to a narrow sector. Existing works coordinate sensing and communication in a time-division manner, which takes advantage of the sector level sweep during the beam training interval for sensing and the data transmission interval for communication. Beam training is a low frequency (e.g., 10Hz) and low duty-cycle event, which makes it hard to track fast movement or perform continuous sensing. Such time-division designs imply that we need to strike a balance between sensing and communication, and it is hard to get the best of both worlds. In this paper, we try to solve this dilemma by exploiting side lobes for sensing. We design *Sidense*, where the main lobe of the transmitter is directed towards the receiver, while in the meantime, the side lobes can sense the ongoing activities in the surrounding. In this way, sensing and downlink communication work simultaneously and will not compete for hardware and radio resources. In order to compensate for the low antenna gain of side lobes, *Sidense* performs integration to boost the quality of sensing signals. Due to the uneven side-lobe energy, *Sidense* also designs a target separation scheme to tackle the mutual interference in multi-target scenarios. We implement *Sidense* with Sivers mmWave module. Results show that *Sidense* can achieve millimeter motion tracking accuracy at 6m. We also demonstrate a multi-person respiration monitoring application. As *Sidense* does not modify the communication procedure or the beamforming strategy, the downlink communication performance will not be sacrificed due to concurrent sensing. We believe that more fascinating applications can be implemented on this concurrent sensing and communication platform.

CCS Concepts: • **Human-centered computing** → **Ubiquitous and mobile computing**; • **Hardware** → *Wireless devices*.

Authors' addresses: [Qian Yang](#), Southern University of Science and Technology, Shenzhen, Guangdong, China and Peng Cheng Laboratory, Shenzhen, Guangdong, China, [yangq2022@mail.sustech.edu.cn](mailto:yangq2022@mail.sustech.edu.cn); [Hengxin Wu](#), Southern University of Science and Technology, Shenzhen, Guangdong, China, [wuhx2021@mail.sustech.edu.cn](mailto:wuhx2021@mail.sustech.edu.cn); [Qianyi Huang](#), Sun Yat-sen University, Guangzhou, Guangdong, China and Peng Cheng Laboratory, Shenzhen, Guangdong, China, [huangqy@pcl.ac.cn](mailto:huangqy@pcl.ac.cn); [Jin Zhang](#), Southern University of Science and Technology, Shenzhen, Guangdong, China and Peng Cheng Laboratory, Shenzhen, Guangdong, China, [zhangj4@sustech.edu.cn](mailto:zhangj4@sustech.edu.cn); [Hao Chen](#), Peng Cheng Laboratory, Shenzhen, Guangdong, China, [chenh03@pcl.ac.cn](mailto:chenh03@pcl.ac.cn); [Weichao Li](#), Peng Cheng Laboratory, Shenzhen, Guangdong, China, [liwc@pcl.ac.cn](mailto:liwc@pcl.ac.cn); [Xiaofeng Tao](#), Beijing University of Posts and Telecommunications, Beijing, China and Peng Cheng Laboratory, Shenzhen, Guangdong, China, [taoxf@pcl.ac.cn](mailto:taoxf@pcl.ac.cn); [Qian Zhang](#), Hong Kong University of Science and Technology, Hong Kong, China, [qianzh@cse.ust.hk](mailto:qianzh@cse.ust.hk).

Permission to make digital or hard copies of all or part of this work for personal or classroom use is granted without fee provided that copies are not made or distributed for profit or commercial advantage and that copies bear this notice and the full citation on the first page. Copyrights for components of this work owned by others than ACM must be honored. Abstracting with credit is permitted. To copy otherwise, or republish, to post on servers or to redistribute to lists, requires prior specific permission and/or a fee. Request permissions from [permissions@acm.org](mailto:permissions@acm.org).

© 2022 Association for Computing Machinery.

2474-9567/2022/12-ART191 \$15.00

<https://doi.org/10.1145/3569498>

Additional Key Words and Phrases: mmWave, 60 GHz, Integrated Sensing and Communication, 6G

### ACM Reference Format:

Qian Yang, Hengxin Wu, Qianyi Huang, Jin Zhang, Hao Chen, Weichao Li, Xiaofeng Tao, and Qian Zhang. 2022. Side-lobe Can Know More: Towards Simultaneous Communication and Sensing for mmWave. *Proc. ACM Interact. Mob. Wearable Ubiquitous Technol.* 6, 4, Article 191 (December 2022), 34 pages. <https://doi.org/10.1145/3569498>

## 1 INTRODUCTION

As the sub-6GHz spectrum is getting overcrowded, we are turning our attention to the millimeter wave (mmWave) band, where there is plenty of spectrum available. 802.11 ad/ay in the mmWave band supports up to 2 GHz bandwidth and achieves data rates above 7 Gbps [10, 11]. 5G is also exploring the mmWave band for high-speed transmission. At the same time, mmWave also has superior performance for sensing, thanks to its nature of short wavelength, large antenna array, and huge bandwidth. Previous works have shown that we can use mmWave for indoor mapping, tracking, and material sensing [27, 49–51]. Thus, it is a hot trend to consider the joint design of sensing and communication in the mmWave band, where we can exploit its capability to the full extreme.

However, in mmWave communication, the transmitter uses beamforming to concentrate the transmission power towards the receiver, combating the high path loss. Unlike the omnidirectional antenna in sub-6G WiFi, in 802.11 ad/ay, the pencil-like communication beam limits the sensing range. Existing mmWave sensing systems perform sensing within the beam training period [29, 33], during which the AP sequentially directs the transmission beams towards different angles. By analyzing the reflected signals, we can track the target at each angle. The beam training period is originally designed to find the best-aligned beam pattern between the AP and stations. Following the beam training phase is the data communication phase, where the matched beam pattern is used for directional communication. Beam training is a low frequency (e.g., 10Hz) and low duty-cycle event, which makes it hard to track fast movement or perform continuous sensing. This brings the dilemma between sensing and communication in the mmWave band. When the AP is performing beam training, it can sense the environment but no data communication; when the AP and stations are communicating, the directional transmission constrains the sensing scope to a specific sector.

Different from the above time-multiplexing strategy, multi-beam solutions are proposed [3, 6, 34, 60], where there is a fixed directional beam for downlink communication, and the other sweeping beam for sensing. With multi-beam design, we can support simultaneous sensing and downlink communication. However, the additional

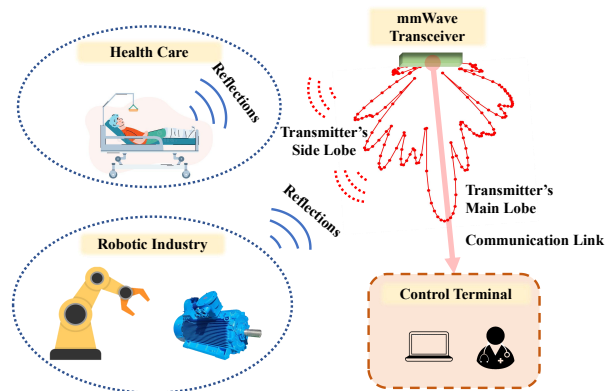


Fig. 1. *Sidense* overview. *Sidense* performs directional data transmission (with the transmitter's main lobe) and omnidirectional sensing (with the transmitter's side lobes).

sensing beam may impede the spatial diversity of directional transmission, causing interference to other devices on the same channel. Moreover, the transmission power is shared between the communication and sensing beams, and thus the communication link SNR would decline.

We ask the question, can we achieve simultaneous downlink communication and sensing, without degrading the communication performance? We observe that, in directional transmission, while the most of power is concentrated towards a desired direction, the remaining power is distributed over all angles, i.e., side lobes. We can use these side lobes for sensing. Side lobe based sensing will neither reduce the main lobe power nor cause extra interference. Thus, it will not degrade the communication performance.

Although the idea of side lobe based sensing sounds simple, it is not straightforward to achieve this goal. There are three challenges need to be tackled. First, the energy of side lobes is always much lower than the main lobe. Theoretically, for the rectangular aperture antenna, the first side lobe is  $-13.26$  dB weaker than the main lobe [38]. To better understand the side lobe energy distribution, we collect and analyze two different commercial 60GHz mmWave antennas' predefined beam patterns over the  $[-60^\circ, 60^\circ]$  field of view (FoV) (please refer to Section 3.2.1 for details). We compare the gap of antenna gain between the main lobe and other angles. From Fig. 5, we can see that for more than 50% of the angles in FoV, the antenna gain is 16dB lower than the main lobe; at some certain angles, the gap increases to 30dB. When the weak signals propagate in the air, get reflected by the targets, and propagate back to the AP, the weak target echoes may be overwhelmed by noise. This is a critical challenge for designing a side lobe sensing system.

Second, it is hard to decouple the mutual interference among multiple moving objects. Although it is a well-recognized challenge in RF sensing, this problem is more pronounced in this scenario. As the transmission power has a large variation across the angles, the signals reflected by targets at different angles will also have a large difference in strength, not to mention the diversity in targets' Radar Cross Sections (RCS). Weak reflections may be buried in strong reflections (e.g., reflections from the main-lobe direction), leading to a high target miss rate.

Last but not least, as a common practice in mmWave communication, the AP's beam direction will track the client when the client moves. When the AP switches to a new beam pattern, the signal power distribution among all angles will also change. This will disturb the sensing process where the application requires continuous monitoring.

In this paper, we take the following steps to address the above challenges:

**Adaptive Coherent Integration:** To compensate for the low side lobe power, we take advantage of coherent integration, which is widely used in radar signal processing. With the knowledge of transmitter beam patterns, we perform adaptive coherent integration, where the integration window length is subject to side lobe power. Weak lobes will have a long integration window to boost SNR.

**Signal Separation and Reconstruction:** To extend to multi-target monitoring, we first reshape the receiver beam to suppress the signal from undesired directions. Then we explore the mixture model for multi-target signals. We show that the mixed-signal vector is the linear superposition of each component. We reformulate this problem as Blind Source Separation. We group the observed reflections at adjacent distances and separate them with Independent Component Analysis (ICA).

**Dynamic Background Removal:** To address the dynamics of transmitter beam patterns, we propose a time interleaving manner to remove the background static clutters and avoid interruption to continuous sensing.

In this paper, we design *Sidense*, a mmWave platform that is capable of simultaneous sensing and downlink communication. *Sidense* explores the sensing capability of side lobes, which neither cause extra interference nor decrease the power of the main lobe. Thus, *Sidense* performs sensing without sacrificing communication performance. We summarize our contributions as follows:

- We design *Sidense*, a mmWave transceiver that can perform directional communication and omnidirectional sensing simultaneously, where the main lobe steers towards the associated station for downlink communication and the side lobes provide omnidirectional sensing coverage.
- We design packet integration and multi-target decoupling schemes to tackle the low, non-uniform antenna gain of side lobes. Packet integration can boost the low-quality sensing signals and multi-target decoupling can recover sensing signals for each individual target. We also handle the dynamics of the transmission beams to achieve continuous sensing.
- We implement *Sidense* with Sivers 60GHz mmWave module. We extensively test the performance of *Sidense* under different conditions. Results show that *Sidense* can achieve robust sensing performance given the weak side lobes. *Sidense* can achieve millimeter motion tracking accuracy at 6m. We also showcase the capability of *Sidense* with a multi-person respiration monitoring application.

## 2 BACKGROUND

Before we present the design for *Sidense* system, we first give a brief overview of the mmWave communication process. While the process is similar for all mmWave communication systems, we present the details according to IEEE 802.11ad. Another name for 802.11ad is DMG, short for Directional Multi-Gigabit. As shown in Figure 2, the DMG Basic Services Set (BSS) transmission time is made up of consecutive beacon intervals [28], and for each beacon interval, it can be separated into two subsets: Beacon Header Interval and Data Transmission Interval.

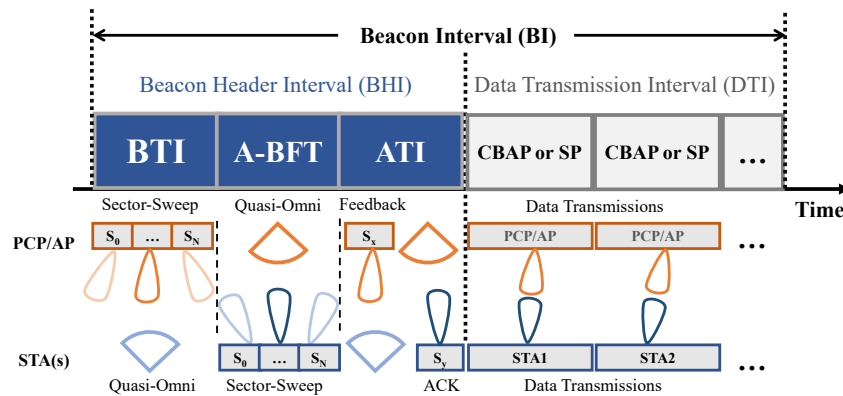


Fig. 2. Directional Multi-Gigabit beacon interval.

**Beacon Header Interval (BHI):** The main purpose of BHI is to align the beam direction of the AP and clients so that the communication links have high SNRs to support multi-gigabit data rates. At the beginning of the BHI, the AP and clients will perform the sector-level sweep to align their communication beams. It works as follows: First, during the Beacon Transmission Interval (BTI), the AP acts as an initiator and uses a narrow beam to sweep in all directions. In each beam direction, it will transmit a DMG beacon frame that contains the sector (or beam) ID. At the same time, the clients (responders) use a quasi-omnidirectional beam to keep listening and record the sector ID with the highest Signal to Noise Ratio (SNR) value.

Next, during the Association Beamforming Training Interval (A-BFT), the role is reversed. The AP uses a quasi-omnidirectional beam to keep listening while the client uses a narrow beam to sweep. In this procedure, clients will randomly select a sector sweep (SSW) slot to perform the sweeping. Before the end of each slot, the AP and client will inform the best quality sector ID to each other by the SSW-Feedback and SSW ACK.

The last step in the BHI is the Announcement Transmission Interval (ATI), during which the AP and clients will exchange requests and responses to initiate and schedule the following data transmission.

**Data Transmission Interval (DTI):** For DMG STAs, the AP allocates the channel access for each client in scheduled time slots. If the DMG STA maintains the beam direction during the data transmission, the interval between two data frames is particularly small, only around  $1 \pm 0.1\mu\text{s}$  [28].

There are two different modulation schemes defined in DMG for data transmission. One is single carrier (SC) PHY, which is mandatory in 802.11ad/ay devices; the other one is OFDM PHY, which can provide a higher transmission rate but is optional. Both have the same packet structure and single carrier modulated preamble. The preamble in each transmission packet serves the purpose of frequency offset estimation and channel estimation.

**Dilemma in mmWave Sensing:** In BHI, the sector-level sweep can scan the environment and thus perform RF sensing. Existing mmWave sensing systems (e.g., [29]) exploit the BHI for sensing purposes. In the DTI, the AP uses the directional beam for communication, and the sensing scope is limited to the direction of the main lobe. The BHI is a very short period compared with the DTI, which usually lasts for 1ms in every 100ms. The low sample rate (i.e., 10Hz) and low duty-cycle cannot satisfy the requirement of many applications, such as fast motion and continuous sensing. This is indeed a time-division manner for coordination, which implies that we need to strike a balance between sensing and communication, and it is hard to get the best of both worlds. If we want more time for data transmission, the sensing period/frequency will be suppressed; if we want continuous sensing updates, the communication process will be frequently interrupted. In the rest of this paper, we will present *Sidense*, which enables simultaneous sensing and communication.

### 3 EXPLORE SIDE LOBES FOR SENSING

In this section, we first present the signal model for side lobe sensing and introduce notations that will be used for the following discussion. Then we present the sensing model of *Sidense* and illustrate the challenges that come with side lobe sensing.

#### 3.1 Signal Model for *Sidense*

The commercial 60GHz communication devices usually use *analog phased arrays*, where beamforming is accomplished by adjusting the weight (phase) of the signal in each antenna element to steer the beam direction. This group of weight vectors, called codebook, is usually predefined and stored in the hardware.

Consider two linear phased antenna arrays, the transmitter (TX) and the receiver (RX). We use  $G_t(\theta)/G_r(\theta)$  to denote the TX/RX antenna gain at angle  $\theta$ . Assume that there are  $L$  propagation paths between the TX and RX. For the  $l$ -th path, let  $\alpha_l$  denote the signal attenuation,  $\theta_l$  denote the Angle of Arrival (AoA),  $\phi_l$  denote the Angle of Departure (AoD). The Channel Impulse Response (CIR)  $h(t)$  measured at the RX can be represented as:

$$h(t) = \sum_{l=1}^L \alpha_l G_r(\theta_l) G_t(\phi_l) e^{-j2\pi f_c \frac{d_l}{c}} \delta\left(t - \frac{d_l}{c}\right), \quad (1)$$

where  $d_l$  represents the propagation distance along the  $l$ -th path,  $f_c$  is the carrier frequency,  $c$  is the speed of light and  $d_l/c$  is the signal transmission delay.

As we can see, the received signal strength is related to the TX/RX antenna gain at AoD/AoA. We define  $G_{RT}$  as the integrated antenna gain, which is the integration of TX and RX antenna gain:

$$G_{RT}(\theta_l, \phi_l) = G_r(\theta_l) G_t(\phi_l).$$

When we write the antenna gain in the unit of dB,  $G_{RT}$  can be written as

$$G_{RT}(\theta_l, \phi_l) = G_r(\theta_l) + G_t(\phi_l). \quad (2)$$

For each weight vector in the codebook, it corresponds to different beam directions. We can further expand Equation (2) when considering that the TX and RX can choose any weight vector from the codebook. When the TX antenna array steers towards angle  $\Phi$  and RX antenna array steers towards angle  $\Theta$ , Equation (2) can be written as

$$G_{RT}(\theta_l, \phi_l | \Theta, \Phi) = G_r(\theta_l | \Theta) + G_t(\phi_l | \Phi), \quad (3)$$

where  $G_r(\theta_l | \Theta)$  denotes the RX gain at angle  $\theta_l$  when the beam directs toward  $\Theta$ .  $G_t(\phi_l | \Phi)$  has the similar meaning, but for the TX antenna.

### 3.2 Sensing Model for *Sidense*

In *Sidense*, the mmWave AP serves as a dual-function device. It performs **downlink** data communication with associated clients, while in the meantime, monitoring ongoing activities in the surrounding. As *Sidense* does not modify the communication process of the existing mmWave technology, we focus on introducing how *Sidense* provides the sensing capability. We assume that the AP acts as a monostatic radar, where the TX and RX are co-located, as shown in Figure 3. Please note that in the rest of this paper, we use RX to refer to the receiving chain of the monostatic radar, but not the AP's client. As we do not want to modify the communication procedure, we limit the design space to the RX antenna control strategy and signal processing.

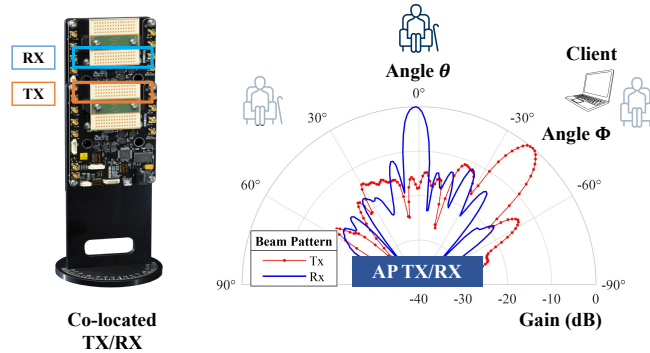


Fig. 3. *Sidense* provides directional communication and quasi-omnidirectional sensing.

The TX beam is directed towards the client (at angle  $\Phi$ ) for communication. When the target is at angle  $\theta$ , outside the main lobe of AP's TX beam, in order to improve the sensing sensitivity, the AP will tune the RX beam towards angle  $\theta$ . The TX/RX antenna gains for the target are  $G_t(\theta | \Phi)$  and  $G_r(\theta | \Theta = \theta)$ , respectively. Thus, the integrated antenna gain turns out to be

$$G_{RT}(\theta, \theta | \theta, \Phi) = G_r(\theta | \theta) + G_t(\theta | \Phi).^1 \quad (4)$$

For simplicity, we can write  $G_{RT}(\theta, \theta | \Theta, \Phi)$  as  $G_{RT}(\theta | \Theta, \Phi)$ . Assume that the target is located at  $-40^\circ$ ,  $1^\circ$  or  $45^\circ$ , and the client is located at  $-40^\circ$ , as shown in Figure 3. Figure 4 shows the beam patterns where the TX main lobe points towards  $-40^\circ$  and the RX main lobe points towards the target. The integrated antenna gains in those object directions are 0dB,  $-18$ dB, and  $-31$ dB, respectively.

Next, we illustrate the challenges that come with side lobe sensing.

<sup>1</sup>The integration gain is averaged over the receiver's half power beam width.

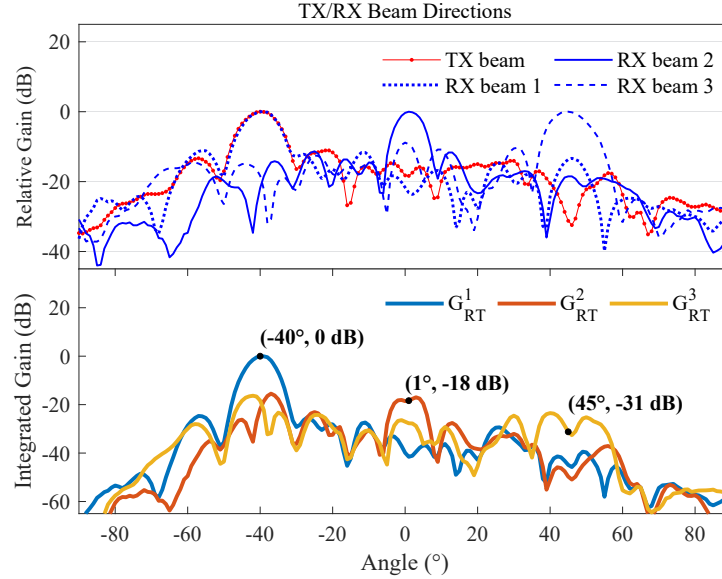


Fig. 4. TX/RX beam pattern in different beam directions and integrated antenna gain for different TX-RX beam pairs.

**3.2.1 Challenge 1: Limited Side Lobes Sensing Range.** As we show above, when the target is at different angles, the reflected signal strengths have large variations. We have strong reflections when the object is at the TX/RX main lobe. As the TX beam is directed towards the client and cannot be controlled for the sensing purpose, we wonder whether the side lobes can substitute the role of the main lobe in sensing.

To understand the gap between the main lobe and side lobes, we analyze the beam patterns for two commodity antenna arrays, i.e., BFM06005 and BFM06010 [41]. Both antennas support a codebook with 63 phase vectors that control the beam steering from  $-45^\circ$  to  $45^\circ$  and the FoV is  $[-60^\circ, 60^\circ]$ . For each phase vector, the manufacturer provides the emitted power distribution within the FoV.

For each TX beam pattern, we rotate the RX beam pattern from  $-45^\circ$  to  $45^\circ$ , as shown in Figure 4. We distinguish between two cases:

- (1) **Case 1:** Sensing with the main lobe. In this case, the TX/RX antenna steers towards the same direction, i.e.,  $\Theta = \Phi$ . We have 63 combinations under this scenario, one for each phase vector in the codebook.
- (2) **Case 2:** Sensing with side lobes. In this case, the TX/RX antenna steers towards different directions, i.e.,  $\Theta \neq \Phi$ . We have  $63 \times 62$  combinations under this case, i.e., 62 TX phase vectors for each RX phase vector.

For each RX beam pattern, we calculate the integrated antenna gain gap between Case 1 and Case 2. The distribution is illustrated in Figure 5. As we note, when we rotate the TX beam, although  $\Theta \neq \Phi$ , the main lobes of TX and RX may overlap when their beam directions are close. This explains the distribution between  $-5$  dB and  $0$  dB. The median value is  $16.04$  dB. It reflects that sensing with side lobes loses  $16.04$  dB gain compared with the main lobe. For 5% of the cases, the gap is larger than  $25$  dB. According to the radar range equation:

$$R = \sqrt[4]{\frac{P_t G_t(\phi_o) G_r(\theta_o) \lambda^2 \sigma}{P_r (4\pi)^3}}, \quad (5)$$

where  $R, P_r, P_t, G_r, G_t, \lambda, \sigma$  denote radar-object distance, received power, peak transmitted power, RX gain, TX gain, signal wavelength, object RCS, respectively. With the same SNR requirement, the low TX gain limits the sensing range. If the gain decreases by 16.04dB, the detection range reduces by 60%.

Note that the beam pattern is related to the antenna type, and thus these statistical results can not represent other types of antennas. However, it generally reflects that sensing with side lobes suffers from signal loss compared with the main lobe.

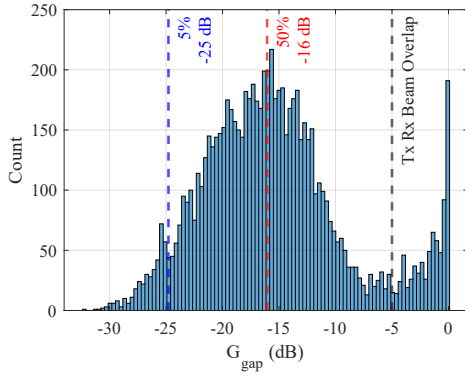


Fig. 5. The distribution of integrated antenna gain difference between Case 1 and Case 2.

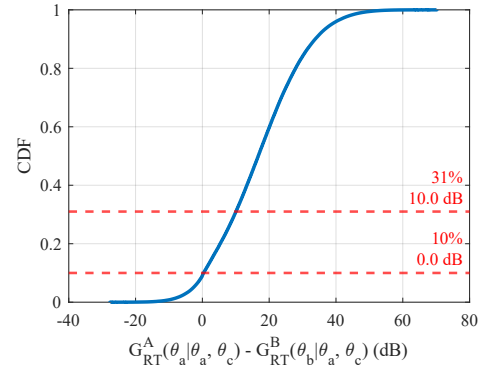


Fig. 6. The distribution of integrated antenna gain difference between the target A and B.

**3.2.2 Challenge 2: Mutual Interference among Multiple Targets.** The mutual interference among multiple moving targets is a well-recognized challenge in RF sensing. This problem is more pronounced in sidelobe sensing.

Assume that there are two moving targets  $A$  and  $B$  at angles  $\theta_a$  and  $\theta_b$ , respectively. They are at the same distance from the AP. The AP is communicating with a client  $C$  at  $\theta_c$ . Thus, the TX beam steers towards  $\theta_c$ . To track the movement of target  $A$ , the AP tunes the RX beam towards  $\theta_a$ . The integrated antenna gain for target  $A$  is

$$G_{RT}^A(\theta_a|\theta_a, \theta_c) = G_r(\theta_a|\theta_a) + G_t(\theta_a|\theta_c).$$

Similarly, the integrated antenna gain for target  $B$  is

$$G_{RT}^B(\theta_b|\theta_a, \theta_c) = G_r(\theta_b|\theta_a) + G_t(\theta_b|\theta_c).$$

As the RX beam is directed towards  $\theta_a$ , we have  $G_r(\theta_a|\theta_a) > G_r(\theta_b|\theta_a)$ . But for the TX beam, we can not determine the relationship between  $G_t(\theta_a|\theta_c)$  and  $G_t(\theta_b|\theta_c)$ . For every possible combination of  $\theta_a, \theta_b$ , and  $\theta_c$  in the FoV, Figure 6 shows the distribution of  $G_{RT}^A - G_{RT}^B$ . Around 31% of cases where  $G_{RT}^A$  is 10.0dB larger than  $G_{RT}^B$ . However, when considering the variety of targets' RCS and distance, it is hard to guarantee that the target  $A$  will have a larger integration gain than target  $B$ , even though the RX beam is directed towards target  $A$ . In the extreme 10% of cases, when the target  $B$  happens to be at TX's main lobe direction, the reflections from target  $A$  may be overwhelmed by target  $B$ .

As the TX/RX antennas are analog phased arrays, they have single input/output. Thus, reflections from all targets are superimposed on the RX side. This makes it hard to decouple the mutual interference between multiple targets.

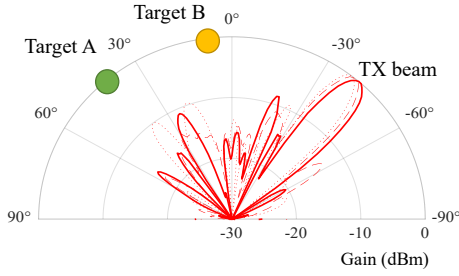


Fig. 7. Experiment setup of TX beam switching.

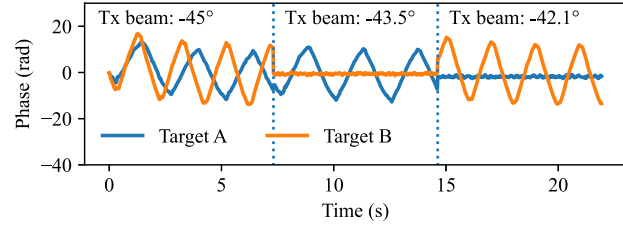


Fig. 8. Target motion waveforms are interrupted by TX beam switching.

**3.2.3 Challenge 3: Interruptions of Continuous Sensing.** To keep the beam aligned for high-speed communication, the AP may switch the TX beam when the client moves. This changes the signal energy on each propagation path and will disturb the continuous monitoring of the target. Here, we show the impact of TX beam switching. As shown in Figure 7, there are two targets  $A$  and  $B$  at angles  $\theta_a$  and  $\theta_b$ , respectively. Both the two targets are moving back and forth at a predefined frequency. Figure 8 shows the signal phase from the channel impulse response. When the TX beam steers towards  $-45^\circ$ , we can clearly track the motion of both targets. However, when the TX beam switches towards  $-43.5^\circ$ , the continuous tracking for target  $B$  is interrupted. When the TX beam switches towards  $-42.1^\circ$ , we can again track target  $B$ , but not target  $A$ . The dynamics of the TX beam will interrupt the sensing process.

When the AP communicates with multiple associated clients or the client is moving, the AP needs to perform frequent beam switching. This will intensify the above problem.

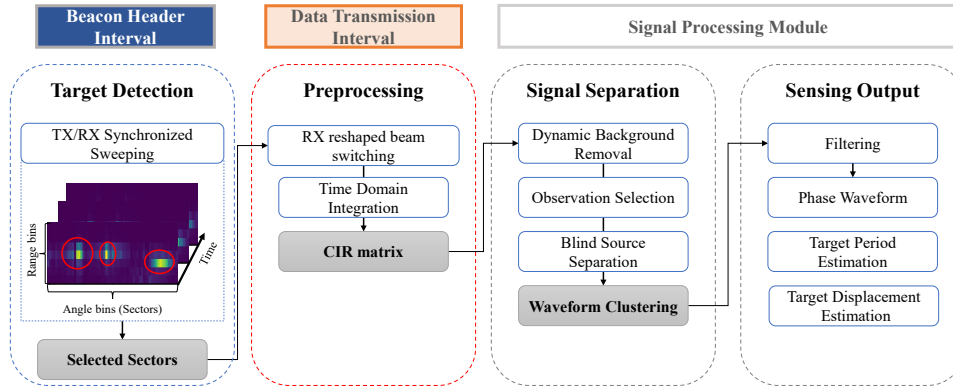
## 4 SIDENSE DESIGN

In this section, we present the system design of *Sidense*. Figure 9 gives an illustration of the system overview. The goal of our design is to achieve robust sensing with side lobes, without affecting the communication performance. The design of *Sidense* is divided into four parts: target detection, preprocessing, signal separation, and sensing output. *Sidense* first detects the presence of moving targets in the beacon head interval. Then during the data transmission interval, *Sidense* performs time-domain integration to increase the sidelobe sensing coverage. After that, *Sidense* uses dynamic background removal to extract the motion-related signal components (dynamic components) and avoid interruptions. To decouple the mutual interference between multiple targets, the dynamic components are further separated and clustered by phase similarity. Finally, *Sidense* outputs the filtered phase waveform and recovers the motion for individual targets.

### 4.1 Target Detection

*Sidense* performs target detection in the beacon header interval (BHI). There are two advantages of utilizing BHI for target detection. First, when the TX/RX steers towards the same direction, the integrated antenna gain is maximized. Thus, we can have a high target detection rate and a large detection range; it can also avoid the non-uniform side lobe gain, which may cause obfuscation in detecting moving targets. Second, the beacon header frame has a longer channel training sequence than the data frame. The STF of the beacon frame is made up of 50 G128 sequences, while the STF of the data frame (single carrier) is made up of 17 G128 sequences. With a longer preamble sequence, we can have a higher SNR for CIR.

During the BHI, the AP performs the sector-level sweep by transmitting beacon frames in each sector. At the same time, AP's co-located RX antenna rotates the beam synchronously with the TX beam. Then *Sidense*

Fig. 9. Signal processing flow in *Sidense*.

extracts the CIR information  $h(t)$  from the reflected packets on each beam direction (sector). To detect the moving target, we calculate the signal variance per range-angle bin over a sliding time window and get the RF snapshots. Figure 10 shows an example of an RF snapshot for one round of sweep. Next, we use the conventional 2D-CFAR [38] to identify the bins with moving targets from the snapshots. We cluster adjacent bins and retain the bin with the highest phase variance as the center of the target.

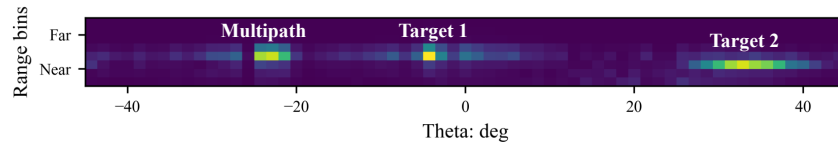


Fig. 10. RF snapshot of Range-Sector Variance.

*Sidense* further adopts majority voting to improve accuracy in target detection. Over a 6-second voting window, when the target is detected for more than a certain threshold (e.g., 25%), *Sidense* decides the presence of a target. For the following data transmission (DTI) in the beacon interval, AP will switch its RX beam among these sectors to track the targets.

Note that the duty cycle of BHI is low, occupying about 1ms in every Beacon Interval (around 102ms) [29]. With such a low sampling rate, we cannot capture fast-moving targets such as quick body motion or machine rotation, whose instantaneous Doppler frequency may be higher than 10Hz [39]. Thus, leveraging the beam training phase for sensing cannot meet the requirements for some applications. In *Sidense*, we utilize BHI for target detection and extend the sensing period to the data communication phase.

#### 4.2 Time Domain Integration

We use  $N_s$  to denote the number of targets identified. During the **downlink** data transmission interval (DTI), the AP directs its TX main lobe towards the client and sequentially switches its RX main lobe among these  $N_s$  sections. The targets are likely to be located outside the main lobe of the AP's TX antenna, and thus the signals that propagate to the targets are emitted by the side lobes. As we mentioned above, the side lobes have much

lower and non-uniform gain. To enhance the sensing signal quality, we borrow the idea of *coherent integration* from radar signal processing [38].

For conventional radar, coherent integration can improve the detectability by accumulating a certain number of pulses within the time-invariant interval (coherence time) [38]. Suppose that there are  $N$  repeated signal samples with white noise. After accumulating these samples in coherence time, the signal power will be amplified by  $N^2$  times, while the noise power increases by  $N$ . The signal SNR after the integration is:

$$SNR_N = \frac{N^2 A^2}{N \sigma_w^2} = N \left( \frac{A^2}{\sigma_w^2} \right), \quad (6)$$

where  $A^2$ ,  $\sigma_w^2$  represent signal power and noise power, respectively. So  $N$  packets accumulation can theoretically improve the SNR by  $N$  times.

We note that the mmWave communication devices have some properties that are favorable for coherent integration. Due to the large bandwidth, compared with sub-6G WiFi, there is a larger number of packets in a short interval and the inter-packet interval is at the microsecond level, which makes it feasible to accumulate multiple CIRs within the coherence time.

However, the communication device is different from radar. Radar pulses are sent at a fixed interval, while the packets are sent by AP at random timestamps. It depends on the upper layer applications. If we set a fixed integration interval, *Sidense* has no idea about how many packets would be accumulated within the interval. To make the problem more complicated, the sidelobes have non-uniform gains. For targets located in different sectors, it requires different integration gains to achieve the same SNR.

In *Sidense*, we design a dynamic sweeping strategy to address the above problems. First, *Sidense* defines a system parameter  $T_I$ , which is the sweeping interval. During the sweeping interval, AP's RX beam sequentially switches among the  $N_s$  target sectors. It actually defines the sampling rate for the sensing function. That is, for every  $T_I$  seconds, the RX beam will scan all sectors for once. Then, *Sidense* will allocate the sweeping interval among the target sectors adaptively according to the integrated antenna gain at that sector. As the phase vectors in the codebook are predefined, we can estimate the integrated antenna gain at each sector (angle). Assume the sensing target is located at angle  $\theta_a$  and the associated client is at angle  $\theta_c$ . The AP will steer its TX beam towards  $\theta_c$  and its RX beam towards  $\theta_a$ . The gap  $G_\Delta(\theta_a, \theta_c)$  between main lobe sensing and side lobe sensing is

$$G_\Delta(\theta_a, \theta_c) = G_{RT}(\theta_a|\theta_a, \theta_a) - G_{RT}(\theta_a|\theta_a, \theta_c).$$

According to the coherent integration theory, if we accumulate  $N$  packets, the SNR improves by  $N$  times [38]. It means that if we want to bridge the gain gap, the required number of packets for accumulation can be calculated from  $G_\Delta(\theta_a, \theta_c)$  by converting decibels to magnitude:

$$N_A(\theta_a, \theta_c) = 10^{\frac{G_\Delta(\theta_a, \theta_c)}{10}}.$$

If both TX and RX antennas have 63 phase vectors in the codebook, there are  $63 \times 63$  TX-RX combinations. We can pre-compute the gain gap for each combination and store the results in a lookup table.

For the  $N_s$  targets, *Sidense* will sort the targets according to the number of required accumulation packets and start with the smallest one. We use Figure 11 to illustrate how *Sidense* works. There are three targets at Sector S1, S2, and S3, respectively. They require  $n_1$ ,  $n_2$ , and  $n_3$  accumulation packets, where  $n_1 \leq n_2 \leq n_3$ . *Sidense* will first switch the RX beam to S1, then S2, and finally S3. Initially, we set a maximum integration time constraint for every target,  $T_1 = T_2 = T_3 = \frac{T_I}{3}$ , which is evenly distributed among the targets to guarantee fairness. It indicates that each target should not occupy the integration interval more than its fair share. Then the AP first steers RX beam towards S1. If either one of the following conditions is met, the AP will switch to the next target:

- (1) AP transmits at least  $n_1$  packets;
- (2) The time allocated for  $S_1$  runs out.

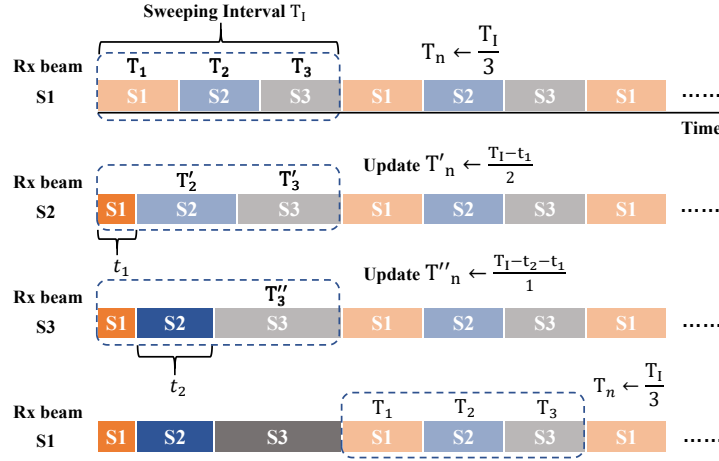


Fig. 11. Schematic of Time Domain Concentration.

If AP transmits packets back-to-back, e.g., streaming high-quality videos, AP will switch to  $S_2$  before the time allocated for  $S_1$  runs out; if AP seldomly transmits packets in the period, AP will switch to  $S_2$  when the time allocated for  $S_1$  runs out.

For the next sector, AP will update the integration time constraint for  $S_2$  and  $S_3$ , by distributing the remaining integration interval evenly between them, ie,  $T'_2 = T'_3 = \frac{T_1 - t_1}{2}$ , where  $t_1$  is the time that RX beam steers towards  $S_1$ . In Case 1,  $t_1 < T_1$ ; in Case 2,  $t_1 = T_1$ . This process continues until all target sectors are scanned.

With such a design, targets with a larger gain gap can have a longer integration interval. As the integration gain is a logarithmic function of the accumulation number, the more packets required, the smaller the marginal gain. While for some weak directions, although there may not have enough packets as we expect, it suffers a minor loss. For example, if 100 packets are required but we only get 50, the integration gain is only 3dB lower than the expected value.

Note that the targets may be located in the null direction in the TX beam pattern. Assuming that the target is 2 meters away from the AP and the surface of the target facing the AP has a width of 20cm, it forms a circular sector with the AP whose central angle is about  $6^\circ$ . As the nulls are usually very narrow and sharp, the target can be radiated with signals from the lobes besides the nulls, as shown in Figure 4. In *Sidense*, as our targets are usually human bodies and industrial robots, their sizes are large enough, so that they can still be detected even in null directions.

### 4.3 Multi-target Signal Separation

According to Eq. (1), the received signal is a linear combination of the multiple propagation paths. We can further distinguish them by static or dynamic paths. The static path, denoted as  $D_s$ , is the propagation path that the signals are reflected by stationary objects in the environment, while the dynamic path  $D_m$  is the propagation path that the signals are reflected from moving objects. According to this propagation characteristic, the CIR in Eq. (1) can be further divided into static component and dynamic component:

$$\begin{aligned}
h(t) &= h_s(t) + h_d(t) \\
&= \underbrace{\sum_{l=1}^{D_s} \alpha_l G_r(\theta_l) G_t(\phi_l) e^{-j2\pi f_c \frac{2d_l}{c}} \delta\left(t - \frac{2d_l}{c}\right)}_{\text{static}} + \underbrace{\sum_{l=1}^{D_m} \alpha_l G_r(\theta_l) G_t(\phi_l) e^{-j2\pi f_c \frac{2[d_l+r_l(t)]}{c}} \delta\left(t - \frac{2[d_l+r_l(t)]}{c}\right)}_{\text{dynamic}}. \quad (7)
\end{aligned}$$

where the  $d_l$  now represents the one-way signal propagation distance on  $l$ -th path. Suppose there are two signals reflected from different moving targets, the dynamic components are  $h_d^{l_1}(t)$  and  $h_d^{l_2}(t)$ , respectively. Figure 12 shows the linear combination relationship for multiple dynamic components in IQ domain. For the

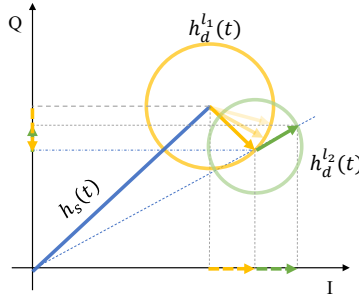


Fig. 12. Signal Composition Model in I-Q domain.

static component  $h_s(t)$ , it can be removed by subtracting the mean value of  $h(t)$  as in [24, 55]. The superimposed signal shows the integrated result of all the moving targets, while the movement of each target is manifested in its own phase variation. Thus, it is necessary to separate the signals for each target.

As the motion of targets are independent of each other, and if the target displacement features are non-Gaussian, this problem can be treated as Blind Source Separation [1]. Following, we illustrate how we address this problem in *Sidense*.

**4.3.1 Observations Selection.** The first step is to select high-quality observations for separation. A time series of observation refers to the signals of a range-angle bin in an RF snapshot (as shown in Figure 10). Although in Section 4.1, we identify the clustering center of the targets, they may not be good choices here. There may exist some motion interference (e.g. rotating fan) that is irrelevant to the target, which can have a large signal variance. So the clustering center in the detection result may be interference. Thus, we need to identify the set of range-angle bins from which we can recover the target movement with high quality.

To select high-quality observations, we use target movement patterns as indicators. For instance, if *Sidense* is tracking human breathing rate, the signal periodicity can be used as an indicator. The normal human breathing rate at rest is 16 – 25 breaths per minute [31]. Accordingly, *Sidense* will select range-angle bins whose power is high within this frequency range. For instance, given the target frequency range  $[f_1, f_2]$ , the frequency ratio indicator  $I_{fr}$  can be represented as:

$$I_{fr} = 10 \log_{10} \frac{\sum_{n=f_1}^{f_2} g[n]}{\sum_{n=1}^N g[n] - \sum_{n=f_1}^{f_2} g[n]}, \quad (8)$$

where  $g[n]$  is the discrete Fourier Transform (DFT) at frequency  $n$ . For non-periodic activities, observations can be selected by a classifier as in prior recognition work [39].

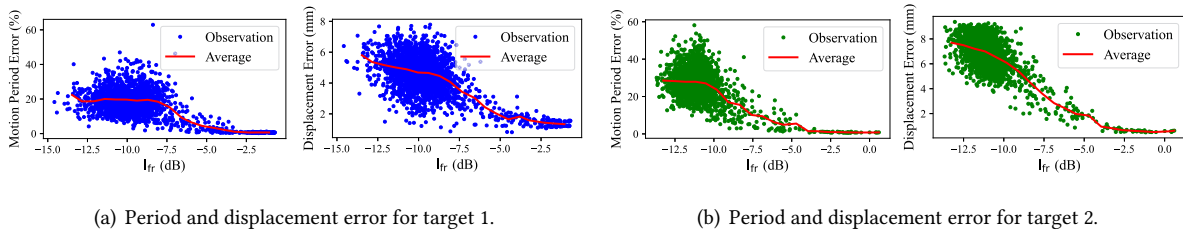


Fig. 13. The observations' perception accuracy versus the frequency ratio indicator.

Take two periodic moving objects as an example. For each target, we collect 4096 observations and evaluate their motion period error and absolute displacement error (for details of evaluation metrics, please refer to Section 6). Figure 13 shows the sensing error for observations with different values of  $I_{fr}$ , where the sensing error decreases as  $I_{fr}$  increases. However, for different targets, the error will converge at different values of  $I_{fr}$ . Thus, a fixed selection threshold may miss observations from some targets. In order to address this problem, we construct three types of observation groups as follows:

- (1) A coarse observation group: select the observation with the top 50%  $I_{fr}$  in each sector. We use a conservative threshold to avoid missing potential high-quality observations.
- (2) A refined observation group: select the observation with  $I_{fr}$  larger than the median value of the coarse observation group, so that the high-quality observations can have more weight in the following processing procedure.
- (3) Coarse observation sub-groups: these sub-groups are formed by selecting signals on every two adjacent range bins of the coarse observation group, for the consideration that reflections from one target may appear in two adjacent bins.

After finishing the selection, the selected signals are assigned to different observation groups, as shown in Figure 14.

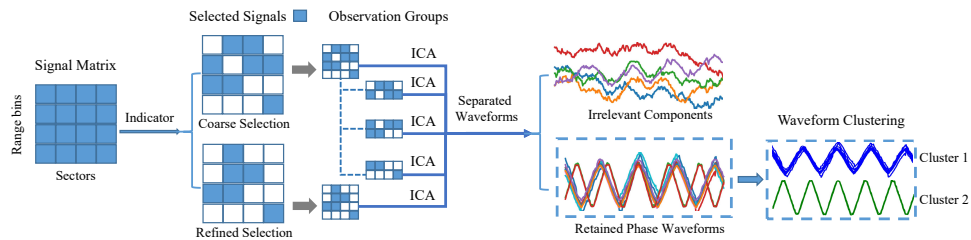


Fig. 14. Signal separation process.

**4.3.2 Waveform Separation and Clustering.** We perform complex JADE ICA [7] on each observation group and get a set of separated components. Since we are interested in the target movement, which is embedded in the phase of signals (as shown in Eq.(7)), we extract the phase information from the separated complex components. As shown in Figure 14, we use  $I_{fr} > -6.5\text{dB}$  to filter out the irrelevant components from the decoupled waveforms, where the threshold is determined empirically. As multiple components may come from the same target, we need to cluster the components that belong to the same target. Since the number of targets is unknown, unsupervised

clustering is utilized. In our case, we use DBSCAN [13], which is widely used in waveform clustering [18]. We define the distance of two phase sequences  $u, v$  as follows:

$$\text{dist}(u, v) = 1 - |\text{PCC}(u, v)| = 1 - \left| \frac{\text{cov}(u, v)}{\sigma_u \sigma_v} \right|, \quad (9)$$

where  $\text{cov}$  is the covariance between the two sequences and  $\sigma_u, \sigma_v$  are their variances. The Person correlation coefficient (PCC) indicates the linear similarity between the two sequences, where a higher correlation represents the higher similarity. The absolute PCC value is always between 0 and 1. After clustering, we flip the component which is negatively correlated in one cluster. Then we average the sequences in the cluster as the target displacement.

#### 4.4 Interference Suppression

As we can see from Figure 4, the integrated gain at the TX main-lobe direction is equal to or even stronger than the target direction. Thus, a moving object in the main-lobe direction will overwhelm the reflected signals from other directions. To suppress the interference from the main-lobe direction, existing works optimize the RX beam pattern to minimize the RX gain in TX main lobe direction [3]. However, due to quantization error and hardware imperfection, the results are not satisfactory when applied to the antenna array.

We adopt the windowing to reshape the RX beam, a straightforward but effective way to increase the Peak to Sidelobe Ratio (PSR). As shown in Figure 15, given a 16-element linear array, the PSR for the conventional beamforming pattern is 13.46dB. After multiplying this antenna weight with a Kaiser window, the PSR increases

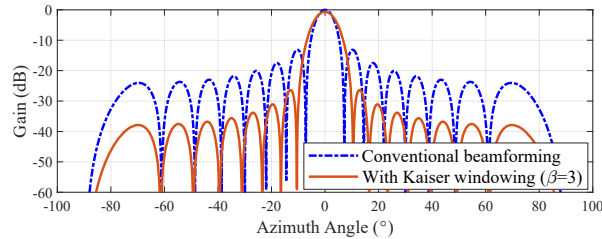


Fig. 15. RX beamforming before and after windowing.

to 25.72dB, further suppressing the signals from unwanted directions. Note that the sidelobe attenuation is affected by the Kaiser window Shape Factor  $\beta$ , a positive real scalar. Increasing  $\beta$  will increase the sidelobe attenuation but will widen the main lobe, which will decrease the angular resolution. Thus, we choose a suitable parameter  $\beta = 3$  to trade off the beam width and the PSR. After windowing, the half-power beamwidth is around  $8.2^\circ$ , only increased by  $2.2^\circ$ . To avoid the decrease of main lobe gain due to windowing, we carried out the antenna amplitude correction. After correction, the main lobe gain decreases by around 0.66dB. According to the radar range equation in (5), the sensing range will decrease by around 3.71%. So the RX beam windowing has negligible effect on sensing coverage and angular resolution.

#### 4.5 Continuous Sensing with Dynamic TX Beams

When the TX beam switches directions, the energy distribution along all angles will change and the sensing process will be interrupted. There are two cases where the TX beam will change direction:

- (1) When the associated client moves, the AP will update the beam direction to track the client;
- (2) When there is more than one client, the AP will steer towards each client in the scheduled time slot.

These cases are inevitable in mmWave communication. According to Eq. (7), when the TX beam pattern switches, the CIR for the propagation paths will change and are no longer coherent before and after switching.

Since *Sidense* works as a mono-static radar, it has the knowledge of the current TX-RX beam combination. Thus, it can perform coherent integration for packets under the same beam configuration. Figure 16 distinguishes two cases. In Figure 16(a), the TX beam does not switch. The sweeping RX beam currently steers towards sector S2.  $t_{m,n}$  represents the integration time under the combination of TX beam  $m$  and RX beam  $n$ . The accumulation will continue until the required packet number is satisfied or the allocated time  $t_{1,2}$  runs out. If the accumulation process is interrupted by the TX beam switching, as shown in Figure 16(b), the remaining allocated time  $t_{2,2}$  will accumulate packets under the new TX-RX beam combination. As the channel condition has changed, packets accumulated during  $t_{1,2}$  and  $t_{2,2}$  will remove the static component, separately. The final integration result is the average of the results from  $t_{1,2}$  and  $t_{2,2}$ .



Fig. 16. Time domain integration when TX switch.

## 5 IMPLEMENTATION

**Hardware Implementation:** We implement *Sidense* with a USRP-2974 and two Sivers EVK06002, where the USRP-2974 works as the controller and the baseband processor, while Sivers EVK06002 works as the mmWave RF unit. Figure 17(a) shows the prototype we built, and Figure 17(b) shows the system hardware architecture. The USRP-2974 has an FPGA and an Intel i7 onboard processor. It supports a maximum bandwidth of 160MHz. In *Sidense*, the USRP generates a 100MHz single carrier signal, which has the same frame format and modulation scheme as IEEE 802.11ad. It transmits about 12,729 packets per second. Note that due to the limitation of hardware, we cannot generate a 2.16GHz, fully 802.11ad-compliant signal. We use this narrow version signal to validate the idea of side lobe sensing.

The Sivers EVK06002 supports a wide frequency range from 57GHz to 71GHz, with 16+16 TX/RX analog phased antenna array. Both TX and RX have an integrated beam book for instant beam steering, with 1 omni-directional and 63 directional patterns ranging from  $[-45^\circ, 45^\circ]$ . As the Sivers EVK06002 is a half-duplex device, to emulate a monostatic radar, we synchronize two Sivers EVK06002 by cascading their 45 MHz internal clocks so that one acts as the radar TX and the other one acts as the radar RX. To avoid misalignment between TX and RX antenna arrays, we stack the TX and RX, with the RX slightly above the TX, as shown in Figure 17(a).

We connect the USRP TRX and RX port to the Sivers EVK06002 transceivers. Since the USRP TRX and RX channel only support a single output/input, to satisfy the EVK06002's four differential IQ inputs/outputs requirement (i.e.,  $I^+$ ,  $I^-$ ,  $Q^+$ ,  $Q^-$ ), we use a 2 way-90 degree power splitter to make the TX stream into two quadrature streams ( $I$  and  $Q$ ), as shown in Figure 17(b). Then we use a differential power splitter to generate two differential inputs ( $I^+/I^-$  and  $Q^+/Q^-$ ). The receiver path is similar, where splitters are replaced with combiners.

A 100MHz single carrier modulated baseband signal is generated by the USRP, then upconverted to 480MHz and fed into EVK06002, which finally upconverts the signal to 60GHz band. The signals are transmitted and received via the 16-element antenna array. The TX and RX beam switch can be triggered by a pulse signal. The index of the beam entry will increment by one when a pulse rising edge comes. We utilize the USRP AUX IO port

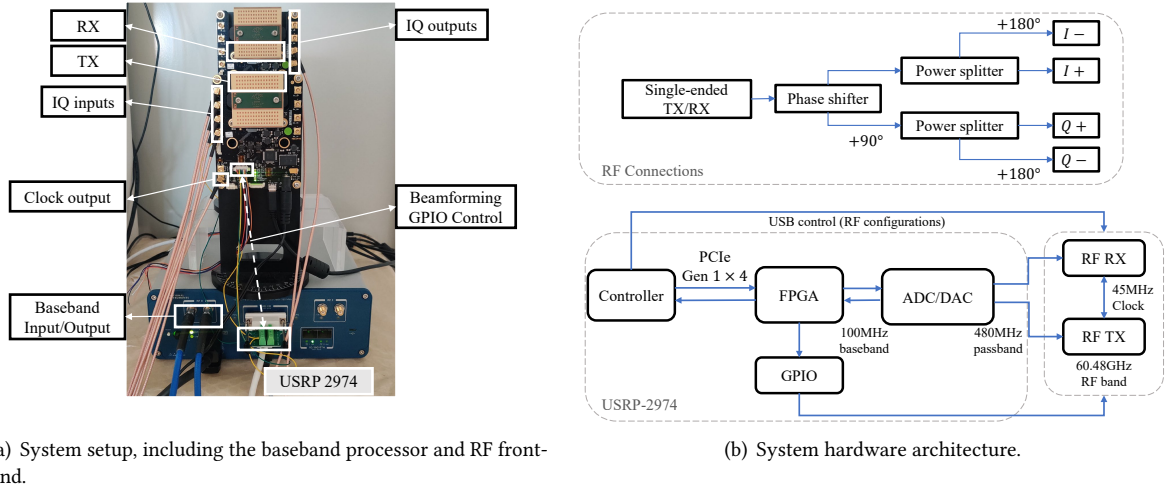


Fig. 17. System prototype.

to send pulses to the EVK06002's GPIO control interface. The minimum beam switch interval is 20ns, and the maximum loading time is 35ns. However, after each beam switch, we found it needs around 1.5ms to get reliable phase readings. So we wait for 1.5ms before extracting CIRs from the preamble sequence.

**Software Implementation:** We implement our algorithm in Python 3.8, with Tx/Rx stream control module from USRP Hardware Driver (UHD) software API. The Siverson's Eder software is used to configure parameters of EVK06002. To save the computation cost, we only process the preamble sequence to get CIRs in real-time and do not decode the payload part.

**Environment and Ground truth:** We conduct our experiment in five real-world indoor environments, including two meeting rooms, two offices, and a balcony seating area (as shown in Figure 28, Figure 18, and Figure 29). In the benchmark experiments, we use several programmable sliding tracks to generate controllable periodic motion, whose displacement precision is  $\pm 0.03\text{mm}$ . The ground-truth breathing rate in the case study is obtained from Vernier Go Direct respiration belt [46]. The sampling rate is set as 80Hz. The starting time between devices is aligned by the Network Time Protocol (NTP), where the synchronization precision is millisecond level.

**Baseline:** We establish a baseline for comparison. In the baseline, the Rx beam sweeps on the same selected sectors with our method. There are three differences: (1) It does not perform time domain integration; (2) It does not perform Blind Source Separation; (3) It does not perform interference suppression (RX beam without Kaiser windowing).

## 6 EVALUATION

In this section, we evaluate the performance of *Sidense* under different scenarios. The sliding track, which carries the target, is programmed to move back and forth at a predefined displacement  $D$  every  $T$  seconds. The sensing accuracy of *Sidense* is evaluated by two metrics:

- (1) The percentage error of motion period  $\left| \frac{T' - T}{T} \right|$ : The motion period is estimated by the time interval between two effective peaks in the motion waveform (e.g., the signal phase).
- (2) Absolute displacement error  $|D - d|$ : According to  $d = \lambda \Delta\phi / 4\pi$ , the displacement  $d$  is calculated from the phase shift  $\Delta\phi$  between the peak and the nearest valley.

At the end of this section, to showcase the sensing capability of *Sidense*, we utilize *Sidense* for vital sign tracking in multi-people scenarios.

## 6.1 System Robustness to Communication Factors

**6.1.1 Impact of Transmitter Beam Direction.** By default, we use a wooden cylinder as the sensing target. Its height and radius are 40cm and 7.5cm. To fully evaluate the influence of transmitter (TX) beam direction, we configure the TX beam to sweep through the predefined 63 weight vectors in the codebook, rotating the beam direction from  $-45^\circ$  to  $45^\circ$ . As shown in Figure 18, we put the object at 5 different angles to the *Sidense* device, at  $-45^\circ$ ,  $-22^\circ$ ,  $0^\circ$ ,  $22^\circ$ ,  $45^\circ$ , respectively. The distance between the device and the target is 2m; the motion period is configured to be 2s. The TX transmission power is set at 22dBm.

The results are shown in Figure 19. Each subfigure corresponds to one target location, where the x-axis represents the TX beam direction. It is supposed that when the Tx beam steers towards the target, we will have good sensing performance. This is validated in the performance of the baseline. Large errors occur when the TX beam direction is far away from the target. When the target is at  $-45^\circ$  and  $-22^\circ$ , the wall can create a rich multipath profile, and more signals can be reflected by the target. Thus, when the target is at these two locations, for the majority of TX beam directions, the error is small. Comparing the baseline and *Sidense*, we can see that *Sidense* has superior performance compared to the baseline. The error of *Sidense* is kept at a low level under all target locations and TX beam directions, which validates that *Sidense* can effectively compensate for the gain gap between the sidelobe and the main lobe, and is robust to different TX beam directions. Figure 20 summarizes the results by target locations. Similarly, we can see that *Sidense* achieves more accurate sensing results than the baseline.

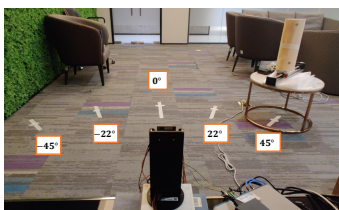


Fig. 18. Experiment setup.

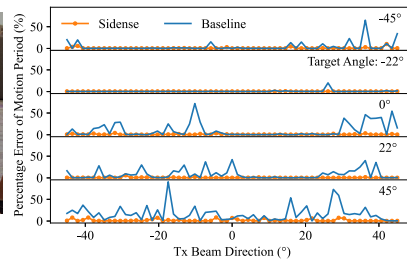


Fig. 19. Impact of Tx beam direction.

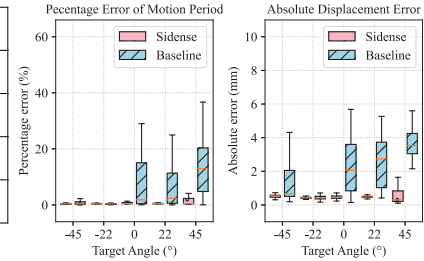


Fig. 20. Impact of Target Locations.

**6.1.2 Impact of Dynamic Transmitter Beam.** We evaluate the sensing performance when the TX beam of *Sidense* is dynamic. We pick three different dwell intervals: (1) 13ms, which represents fast switching between multiple clients; (2) 1.5s, a moving client; (3) 7s, which corresponds to an accidental client move. The TX beam will switch between  $-45^\circ$ ,  $-43.5^\circ$  in (1) and (2), and switch between  $-45^\circ$ ,  $-43.5^\circ$ ,  $-42.1^\circ$  in (3). The interrupted integration is reconstructed by the method mentioned in Sec. 4.5. Here we test with two identical targets (the wooden cylinder, 20cm height and 7.5cm radius), which are 2m away from the *Sidense* device, at around  $7.5^\circ$  and  $37.5^\circ$ , respectively; their motion periods are set to be 2s and 2.46s, respectively. Figure 21 shows the period and displacement error for the two targets. For target A, the median period error are 0.27%, 0.73%, 0.03%, the median displacement error are 0.24mm, 1.75mm, 1.41mm. For target B, the median period error are 0.46%, 0.56%, 0.72%, the median displacement error are 0.35mm, 0.56mm, 0.25mm. We can see that *Sidense* works well under dynamic TX beam. These accuracies are sufficient for the requirement of many applications. But the sensing performance is different between the two targets. The displacement error for target 1 is slighter larger than target 2. This is because

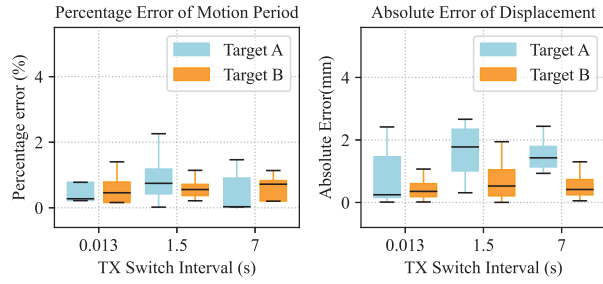


Fig. 21. Transmitter beam switches in different intervals.

the time-domain integration will decrease the sampling rate, for fast movement, it will hurt the displacement resolution. The motion period for target 1 is 2s, shorter than target 2, and thus target 1 has a slightly larger displacement error.

### 6.2 System Robustness to Target Factors

**6.2.1 Impact of Target Distance.** We evaluate *Sidense* under different device-to-target distances (2m to 6m). The experiment setup is shown in Figure 22. Since the target is located at 0°, we repeat the experiment for each Tx beam pattern. The target displacement is configured to be 10mm, and the motion period is 2s. We set the maximum integration window to be 4ms. Figure 23 shows the results for the two metrics. When the target is 2m away, the median error for period and displacement is 0.36% and 0.3mm, respectively. The period error increases with the device-to-target distance, as the propagation loss increases and thus lower SNR for the reflected signals. We observe that the performance on 4m is better than 3m in this setup. We infer that it is due to the environmental factor. As shown in Figure 22, there is more surrounding furniture at 4m than 3m. These furniture may scatter the incident signals and more signals can be reflected by the target.

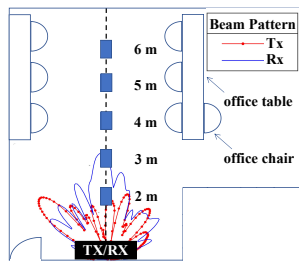


Fig. 22. Experiment setup for evaluating different device-to-target distances.

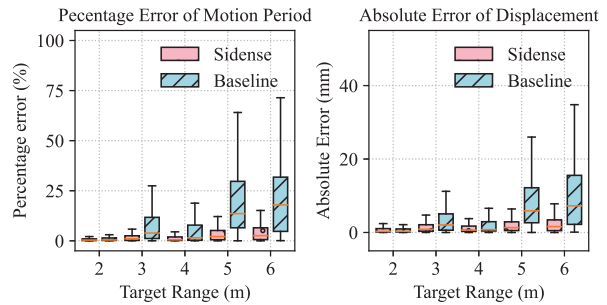


Fig. 23. Perception error for different target distances.

The performance gap between our method and the baseline increases with distance. The 75% error of our method is significantly lower when the device-to-target distance is larger than 3m. The median error for period and displacement is 2.58% and 1.6mm at 6m. It shows that *Sidense* can achieve stable performance with side-lobe sensing.

**6.2.2 Impact of the Separation Angle between Multi-Target.** We evaluate the impact of the separation angle between two targets. In this experiment, the two targets are put 2m away from the device. We put target 1 at  $0^\circ$  and the other target at  $10^\circ$ ,  $20^\circ$ ,  $30^\circ$ , respectively. We also repeat the experiment for each Tx beam pattern. If a target is missed by the target detection procedure (Section 4.1), we set the percentage error of motion period and absolute displacement error to be 100% and 100mm.

The results are shown in Figure 24. The system errors increase when the separation angle decreases. When the targets get closer, the distinguishing capability of RX beamforming declines, and two targets' reflected signals are superimposed. Benefiting from the multi-target signal separation design, *Sidense* performs better than the baseline when two targets get closer. When the separation angle is  $10^\circ$ , close to the  $8.2^\circ$  RX half-power beamwidth (after windowing), the detected targets' clusters will merge, and only the representative sectors will be selected during the target detection. These miss-detection events sometimes happen, deteriorating the sensing performance.

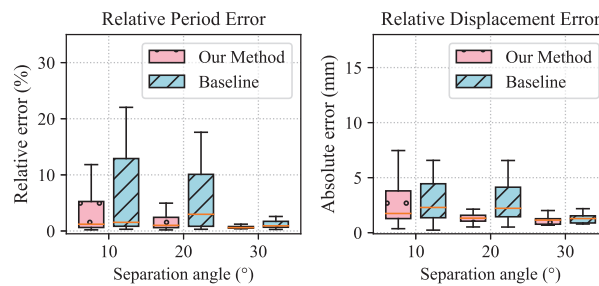


Fig. 24. Performance under different separation angles between the two targets.

**6.2.3 Impact of Target Diversity in Multi-Target Scenarios.** We evaluate the impact of target diversity in multi-target scenarios. The challenge of monitoring multiple targets simultaneously is that reflections from strong targets may overwhelm the reflections from weak targets. Target diversity results from the size of the reflection area, the difference in the device-to-target distance, and the transmitter antenna gain at different angles. We test two-target sensing under three scenarios, gradually increase the gap between the two targets:

- (1) Scenario 1: We use two identical cylinder objects as the targets. They are put at the same distance to the transceiver (i.e., 2m). The separation angle between Cylinder A and Cylinder B is  $30^\circ$ ;
- (2) Scenario 2: Cylinder B is replaced by a cardboard box (Box B) with four times the cross-sectional area as Cylinder B;
- (3) Scenario 3: We move Box B 0.5m towards the transceiver.

For each scenario, we also repeat the experiment for every Tx beam pattern. The statistical results are shown in Figure 25. For *Sidense*, both period error and displacement error do not increase significantly with the gap between targets. The baseline result in scenarios 1 and 2 shows that the increase in target diversity will increase the mutual interference between targets. Although the differences between targets in scenario 3 are larger than 1 and 2, the performance of baseline in scenario 3 is much better. It shows that the appropriate distance separation can make multiple targets more distinguishable in range bins. Compared with baseline, *Sidense* can work well in multi-target scenarios, even when the targets have diverse properties.

### 6.3 System Robustness to Environmental Factors

In this section, we evaluate the *Sidense* performance in different indoor layouts to study the system's robustness to environmental factors. We also evaluate *Sidense* when there is with and without human motion disturbances.

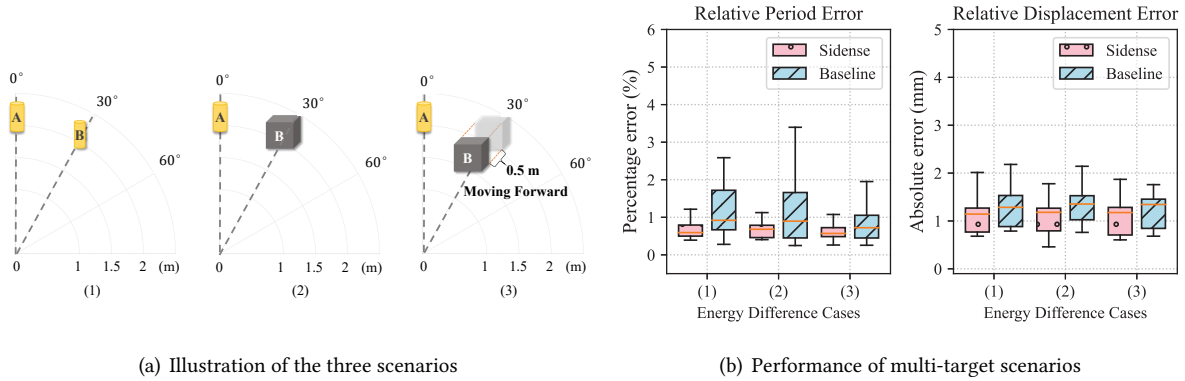


Fig. 25. Impact of the target diversity between multi-target.

**6.3.1 Impact of Different Environments.** We investigate *Sidense* sensing performance in three indoor environments: an office, a meeting room, and a balcony resting area. As shown in Figure 26, we denote each environment by A, B, and C, respectively. The system settings, target size, location and motion mode are nearly identical in these



Fig. 26. Difference indoor environments setup.

environments. The target is a cardboard box with  $12 \times 35\text{cm}^2$  cross-sectional area. The target-to-device distance and angle are around  $(3.8\text{m}, 0^\circ)$  in three environments. The target periodically moves forward and backward towards the device, with a 2s motion period and a 1cm displacement. The TX transmission power is set to be 32dBm. To further understand the indoor multipath effects, we change the furniture layouts, such as computer monitors, chairs, etc., with two different layouts for each environment. We repeat the experiment for 32 Tx beam patterns ( $3^\circ$  angular granularity).

Figure 27 illustrates the result. Compared with the baseline, the environmental impact is not apparent for *Sidense*. When the TX main lobe does not point toward the target, the target is illuminated by the TX side lobes and the environmental multipath reflections. Different indoor layouts will change the multipath energy. Although both the baseline and *Sidense* remove the static multipath component, *Sidense* can effectively enhance the SNR of the side lobe target echoes, which makes it much more robust to different environments.

**6.3.2 Impact of Motion Interference.** We evaluate the performance of *Sidense* under different kinds of motion interference. We choose three different TX main beam directions ( $14.5^\circ$ ,  $15.9^\circ$ , and  $17.4^\circ$ ) and repeat these 3 TX beam settings for each case. The target is located on the AP TX's side lobe. The experiment setup is shown in Figure 28(a), where the target is a cardboard box with  $30 \times 40\text{cm}^2$  surface area, and the distance to the *Sidense* device is 5m. The target is carried by a sliding track to move back and forth every 2s and the displacement is 10mm. We consider four scenarios:

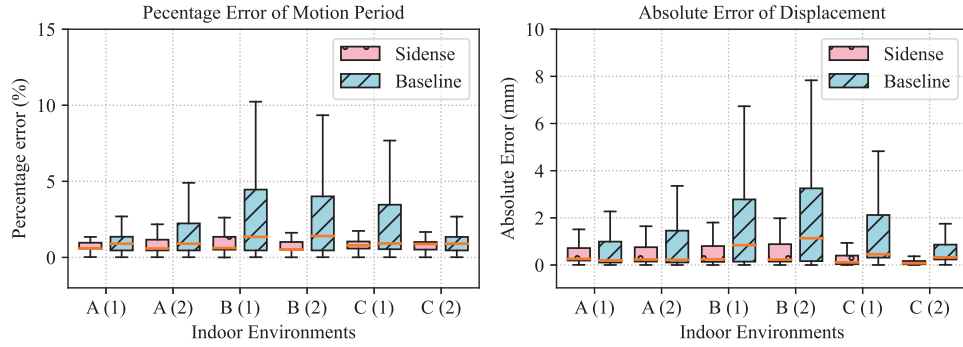
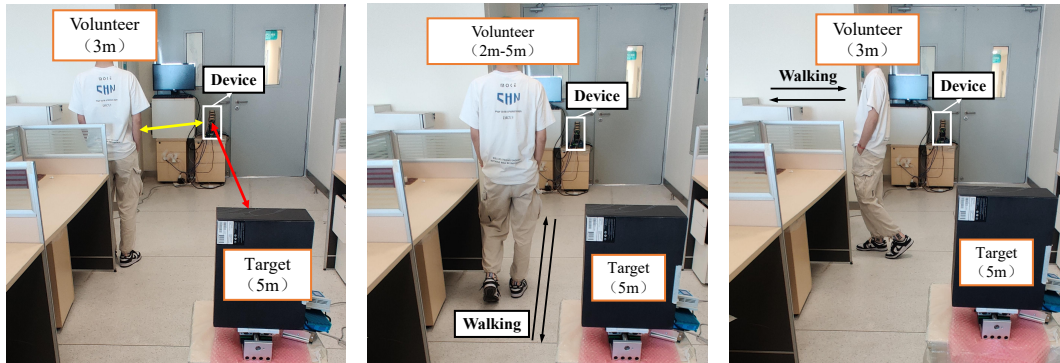


Fig. 27. Performance under different indoor environments.

- (1) Case 1: The volunteer is standing 3m away from the *Sidense* device, at the main lobe direction of the TX beam. The separation angle between the volunteer and the target is around  $16^\circ$ .
- (2) Case 2: The volunteer is at the same location as Case 1 but turns  $90^\circ$  every 3s;
- (3) Case 3: The volunteer is walking at 0.5m/s and the walking path is parallel to the direct path between the device and the target, as shown in Figure 28(b).
- (4) Case 4: The volunteer is walking at 0.5m/s and the walking path is vertical to the direct path between the device and the target, but not blocking the direct path, as shown in Figure 28(c). The angle between the volunteer and the target is at least  $10^\circ$ .



(a) Stable or rotation on the TX main lobe (b) Walking parallel with direct path (c) Walking vertically to direct path

Fig. 28. Environment motion interference setup.

The results are shown in Figure 29. The target detection rates under these four scenarios are 1, 1, 0.84, and 0.93, respectively. Comparing the four scenarios, body rotation on the TX main lobe and walking parallel cause more severe interference. When the volunteer rotates on the TX main lobe, the *Sidense* period error ranges from 0.55% to 6.82%, and the absolute displacement error ranges from 0.11mm to 3.29mm, performing much better than the baseline. This is because the signal-to-noise-plus-interference ratio (SINR) in *Sidense* is improved by

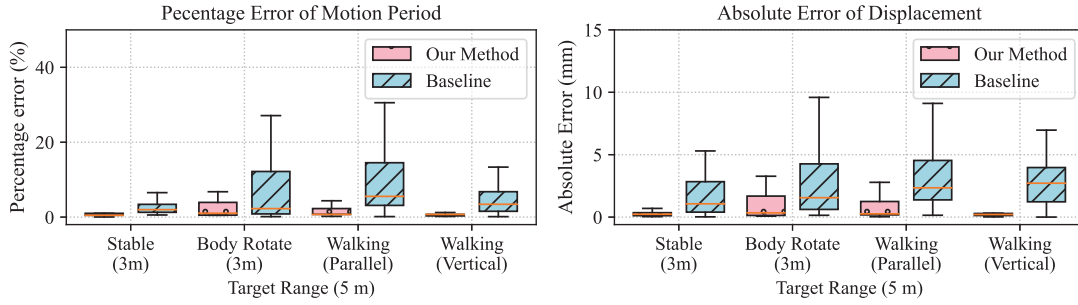


Fig. 29. Sensing performance with motion interference.

the integration gain and the high PSR of the RX beam. The results show that *Sidense* has a relatively stable anti-interference performance.

We further conduct an evaluation of the system's robustness in a more complex indoor layout. As shown in Figure 30, the *Sidense* device is placed in a corner of the  $5 \times 5$  m<sup>2</sup> office room. The target's position relative to the transceiver is (4.2m,  $-10.2^\circ$ ), where the two numbers denote the distance and angle to the AP, respectively. The target periodically moves forward and backward towards the *Sidense* device, and its size and movement mode are the same as described in Section 6.3.1. We consider two sensing scenarios in this office:

- (1) Scenario 1: Relatively static environment, with no additional motion disturbances.
- (2) Scenario 2: Three people are walking or rotating simultaneously, while the range of activities does not block the line-of-sight between the device and the target. As shown in Figure 30(b), one person walks horizontally along the desk, and the other walks vertically along the sofa. The third one sits on the chair and rotates the chair at around (2.3m,  $-20^\circ$ ).



(a) Scenario 1: static environment.

(b) Scenario 2: dynamic environment.

Fig. 30. Environment setup.

The result for Scenario 1 is shown in Figure 31(a). It displays the mean value of motion period error under 63 different TX beam directions, from  $-45^\circ$  to  $45^\circ$ . As for the baseline result, we can see that when TX points to  $[-37.7^\circ, -21.8^\circ] \cup [-13.1^\circ, 5.8^\circ]$ , the sensing performance is better than others. Considering the target angle location is  $-10.2^\circ$ , we can infer that there are multipath and direct paths in these two angular ranges, respectively. However, when the TX main lobe directs towards the monitor (the angular range is about  $[24.6^\circ, 42.1^\circ]$ ), most

of the TX main lobe energy is blocked by LCD monitors, degrading the baseline performance. Comparing the baseline and *Sidense* results, the error of *Sidense* can remain at a low level in most of the TX beam directions, which proves that *Sidense* can effectively compensate for the sidelobe gain and is also robust in complex environments.

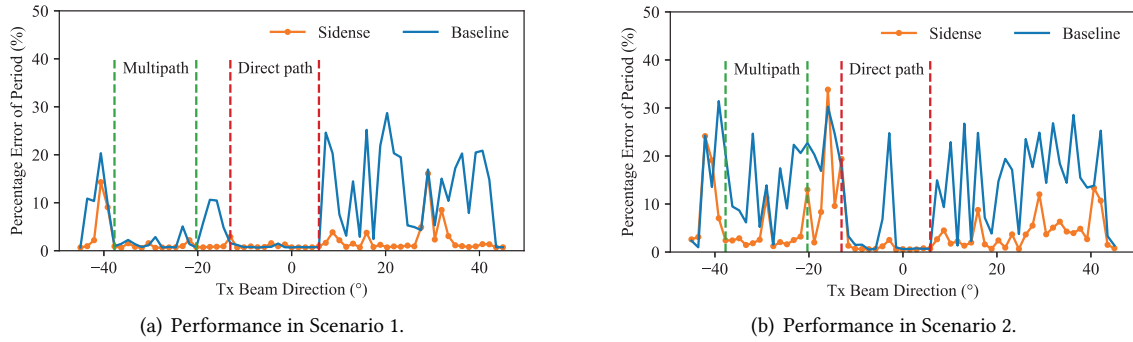


Fig. 31. Performance under different scenarios.

Scenario 2 takes multiple human disturbances into concern, and results are shown in Figure 31(b). Comparing the performance between scenarios with and without interference, the motion interference in the indoor environment will reduce the accuracy of perception. As *Sidense* adopts the windowing to reshape the RX beam and increase the Peak to Sidelobe Ratio (PSR), comparing with the baseline, *Sidense* can provide more interference suppression when the TX main lobe points toward the disturbance source. However, in *Sidense*, since RX beam reshaping will widen the RX main lobe, the interference near the target direction can hardly be suppressed. The overall performance of *Sidense* in Scenario 2 is also better than the baseline.

#### 6.4 Simultaneous Sensing and Down-link Communication Performance

We compare the *Sidense* down-link communication performance when the system is performing joint sensing and communication or solely communication.

**6.4.1 Communication Setup.** The *Sidense* transceiver acts as an AP. As for the client RX, we connect a 60GHz phased antenna array with a USRP 2974 to act as a client RX. We set the baseband sampling rate to 100MHz. To fully investigate the communication performance, we randomly select three different client locations and two kinds of modulation/coding schemes (MCS 9 for QPSK and MCS 12 for 16 QAM). The packet is generated and decoded offline by a Matlab program [30], where each packet's data payload contains 512 data bits. The client captures 20k packets from the AP for each combination of position and modulation type. As the Siverts mmWave RF units suffer from clock drift, we synchronize the client (RX) Siverts clock with the AP's clock via a cable.

**6.4.2 Test Environment Setup.** As shown in Figure 32, the client RX coordinates of the three positions are about  $(1.4m, 20.3^\circ)$ ,  $(1.5m, -29.0^\circ)$ , and  $(1.9m, -29.0^\circ)$ , respectively. We set the RX gain on  $(1.9m, -29.0^\circ)$  to be 3dB lower than the other two locations to enlarge the range distinction of different client locations. The sensing target is located at about  $(4.2m, -10.2^\circ)$ , with a periodic movement of 1cm displacement and 2s period. The beam direction of the AP (TX) and the client (RX) are aligned with each other.

**6.4.3 Simultaneous Sensing and Communication Performance.** Figure 33(a) shows the bit error rate (BER) of MCS 9 and 12. We can see that the communication performance under the two cases, solely communication and joint sensing and communication, is almost the same. The difference of the 95-percentile on the CDF plots is 0 (double

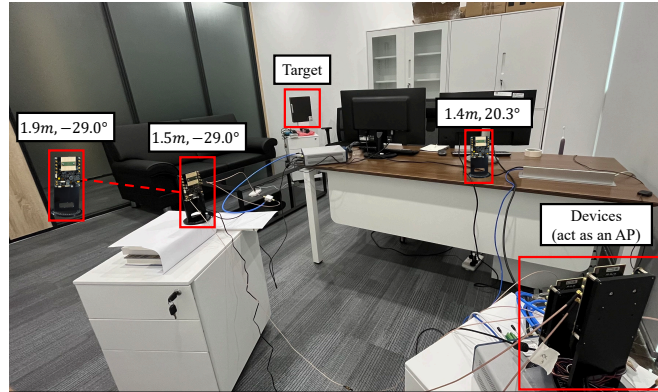


Fig. 32. Experiment setup with simultaneous sensing and communication.

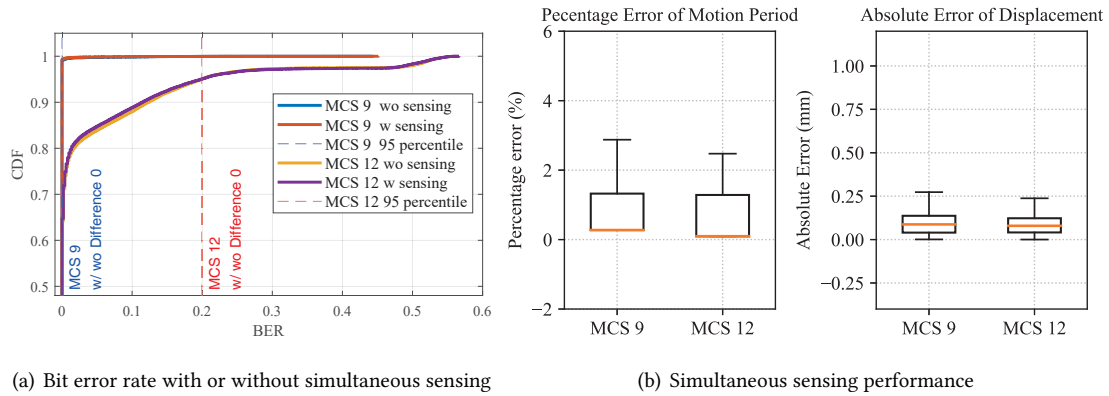


Fig. 33. Sidense performance when performing sensing and communication simultaneously.

precision accuracy). Figure 33(b) illustrates the accuracy of sensing results when AP is performing communication and sensing simultaneously. The median difference between MCS 9 and 12 is not apparent: 0.18% for the motion period error and 0.008mm for the displacement error. Combining the results of Figure 33(a) and Figure 33(b), we can say that Sidense can perform simultaneous sensing and communication, while the performance of down-link communication remains unaffected.

## 6.5 Micro Benchmarks

**6.5.1 Performance of Target Detection.** Since the target detection algorithm will select multiple candidate sectors, we evaluate the validity of sector selection at different distances (2m, 4m, and 6m). For each distance setting, the single target is located at  $0^\circ$  and the target detection test is repeated for 449 times. The statistical result is shown in Figure 34. The results are classified into three categories: LoS-detection, multi-path and miss-detection. For instance, suppose that the target is located at angle  $\theta$ . As the half-power beamwidth of the RX beam is  $8.2^\circ$ , if the selected sectors contain the direction  $\theta \pm 4.5^\circ$ , this selection result will be classified into the LoS-detection group.

If the selected sectors do not contain the direction  $\theta \pm 4.5^\circ$ , they will be classified into the multi-path group. If none of the sectors is selected, it is classified as miss-detection.

Figure 34 shows that when the target is at 2m or 4m, *Sidense* can have nearly 100% target detection rate. The LoS-detection rate decreases at 6m. As the distance increases, the multipath effect will become more evident, as the signals will be reflected by ceilings, floor and furniture. Thus, the target may not be identified from the direct path, but in the multipath profile. While the target may be identified from the multipath profile, the uncertainty of TX beam direction during the communication will degrade the sensing robustness. Thus, it is preferable that the targets are detected on the LoS path.

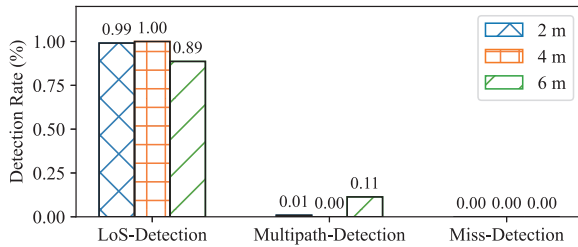


Fig. 34. Target detection rate.

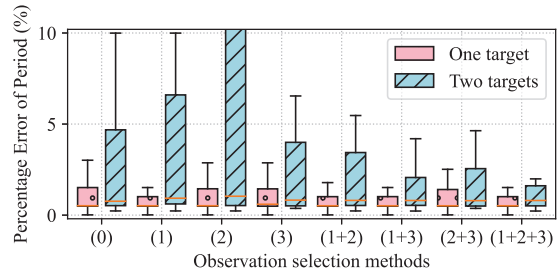


Fig. 35. Performance of different selection metrics.

**6.5.2 Performance of Observation Selection.** We evaluate the *Sidense* single-target and two-target sensing performance for different observation selection methods (described in Sec. 4.3.1). To amplify the influence of mutual interference, the two targets have the same distance from the device. The two targets' data contain two scenarios: (a) TX points to one of the targets; (b) TX does not point to any of these targets. The selection methods we compared are:

- (0) Signal matrix without selection: all of observations are treated as one group.
- (1) Coarse observation selection: select the observations with top 50%  $I_{fr}$  in the signal matrix.
- (2) Refined observation selection: select the observations with  $I_{fr}$  larger than the median value of the coarse observation group.
- (3) Coarse observation subgroups: each subgroup consists of two adjacent range bins in the coarse observation group, considering that reflections from one target may appear in two adjacent bins.

Each methods generate one group (method 0,1,2) or some subgroups (method 3). The signal separation is performed on each group or subgroup. We also evaluate the performance of different combinations of these methods. As shown in Figure 35, the difference is mainly manifested in the two-target scenario since one of the targets is sometimes missing in Scenario (a).

As for the sensing performance of a single target, comparing methods 0 and 1, an appropriate observation selection improves the sensing accuracy. However, comparing methods 1 and 2, when the refined selected signals all belong to the same target, and the source number of ICA is much larger than the actual target number, the separation will slightly reduce the sensing accuracy. As for the two-target scenario, the sensing error of methods 0, 1, and 2 increases in turn since the selection of observation sometimes may result in target miss detection. Method 3 performs better than methods 0, 1, and 2, because it can handle the mutual interference when the two targets' echoes have a similar distance to the device. Therefore, a single metric is challenging to guarantee that all target observations are selected while filtering out the poor-quality observations. Thus, we adopt the combination of them (1+2+3).

## 6.6 Case Study: Multi-person Respiration Monitoring

To showcase the capability of *Sidense*, we use *Sidense* to monitor the respiration rate in multi-person scenario. As shown in Figure 36, three volunteers sit 2.3m from the device and wear the GoDirect respiration sensor to record the ground truth. Person 1 and 2 are separated by  $15^\circ$ , while person 2 and 3 are separated by  $24^\circ$ . The TX main lobe directs towards person 1. *Sidense* first detects the target location and then performs continuous sensing. The output waveforms are filtered by a  $[0.2, 0.6]$ Hz bandpass filter. Figure 37 shows the respiration waveform and ground truth for each person. We can see that the waveform variation of *Sidense* is close to the ground truth. During the 150s' respiration monitoring, the absolute Breath Per Minute (BPM) errors for the three volunteers are 2.1BPM, 0BPM, and 0BPM, respectively.

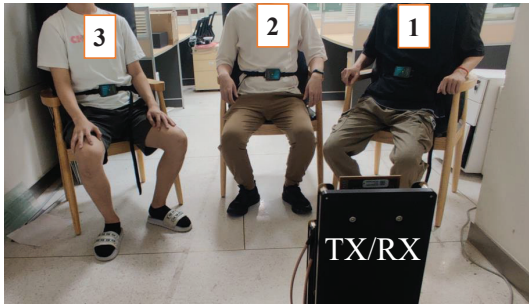


Fig. 36. Multi-people respiration scenario.

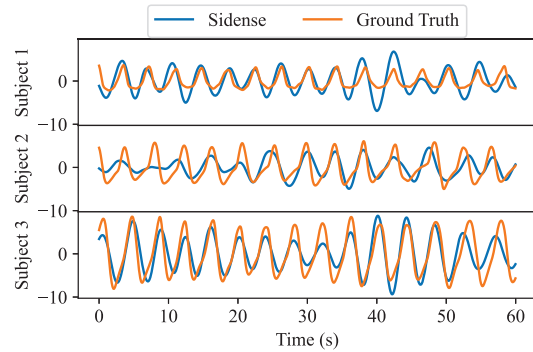


Fig. 37. Respiration waveform.

We also evaluate the performance of the different number of people. Volunteers sit at 2.3m from the device and are separated by  $18^\circ$ . The TX main lobe does not direct towards anyone. Figure 38 shows that the median BPM errors for single, two, and three people are 0, 0.68, and 1.12, respectively. The sensing accuracy decreases as the number of people increases.

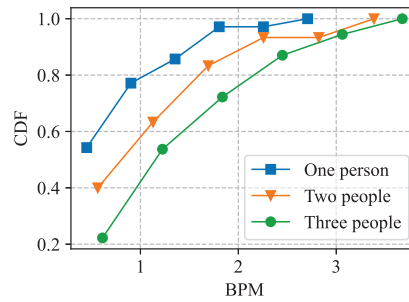


Fig. 38. Performance for the different number of people.

ViMo [48], the state-of-the-art respiration monitoring system using 60GHz WiGig, achieves sensing by configuring the AP in radar-like mode. In ViMo, the median error for one person at 2m is 0.22BPM. For the multi-user scenario in ViMo, when the user-to-device distance is 1m and the separation angle between two people is  $30^\circ$ , the median error ranges from 0.15 BPM to 1.14 BPM. We can find that the accuracy of *Sidense* is comparable to ViMo, while *Sidense* can support concurrent mmWave sensing and communication.

## 7 RELATED WORK

### 7.1 Integrated Sensing and Communication in mmWave Band

In order to reduce the hardware cost and improve spectrum efficiency, the integrated sensing and communication (ISAC) has become a hot research subject. *Sidense* is related to recent works on communication-centric mmWave ISAC designs.

MmWave communication is usually directional, where the energy is focused towards the receiver to combat the high path loss. Some of the existing research assumes that the sensing target falls within the coverage of the communication beam [16, 21, 22, 45], which limits the sensing scope to the communication sector. Beam scanning can extend the sensing scope but cannot maintain directional communication. The time-division multiplexing strategy can schedule directional communication and omnidirectional sensing in different time slots. The time-division multiplexing strategy can be implemented via two approaches, Sector-Level-Sweep [5, 17, 29] and radar-like mode [48, 50, 51]. In Sector-Level-Sweep based method, the device takes advantage of the beam training phase (sector level sweep) for sensing. For instance, mTrack [49] demonstrates short-range (1m) object motion tracking in millimeter precision. POLAR [29] achieves centimeter precision for indoor passive object localization. In addition to the fundamental networking function, 802.11ad chipset also offers a radar-like mode. To perform sensing, the AP is configured to work in the radar-like mode. During the radar-like mode, mmTrack [50] and mmEye [59] implement digital beamforming to perform indoor tracking and imaging, respectively. However, these methods confront a trade-off between the sensing resolution and the transmission efficiency. There are some indoor sensing applications that require a 200Hz - 1kHz slow-time axis sample rate [14, 49, 56, 58], and one sample needs one round of beam sweeping. As the current millimeter wave communication is mainly designed to support high bandwidth applications, such as AR/VR, 4k high-definition video streaming [12], which are sensitive to delay. Frequent communication interruptions will degrade the network quality of service. Different with aforementioned methods, *Sidense* takes advantage of the side-lobe energy in the TX radiation pattern, so it can support concurrent communication and sensing. As for the sensing performance, existing mmWave-based ISAC systems can capture the millimeter-level displacement in the indoor range of 1 ~ 2m [37, 48, 49]. *Sidense* can achieve a similar level of accuracy.

Another direction is the multibeam strategy, which usually generates two beams, with one beam for directional communication, and another beam scanning all directions for sensing [3, 4, 6, 60]. Multibeam strategy can support simultaneous communication and sensing, and it usually jointly optimizes TX and RX beamformers to maximize the target echo SINR, so theoretically, the interference suppression will perform better than *Sidense*. However, in most of the multibeam optimization algorithms, the convergence time is an uncontrollable factor, and lacks real-time validation on practical hardware. Besides, since the energy is allocated between two directions, the antenna gain of the communication beam is reduced, and the sweeping sensing beam may cause interference to other devices in the same environment. Different from the existing multibeam strategy, *Sidense* does not need to modify the original antenna beam pattern, and it takes advantage of the side-lobe energy in the radiation pattern of antenna arrays, which will not decrease the main lobe power nor cause extra interference in the environment.

### 7.2 RF-based Indoor Sensing

Our work is related to existing works on RF-based indoor sensing. According to the sensing device employed, related works can be grouped into the following two categories.

**7.2.1 Radar-based Sensing.** A number of indoor sensing applications have been implemented based on radar devices, including frequency-modulated continuous-wave (FMCW) radar, continuous-wave (CW) Doppler radar, and ultra-wideband (UWB) pulse radar. Given the large bandwidth, radars can be used for fine-grained motion measurements, including indoor positioning [2], gesture recognition [26], human skeleton tracking [61, 62],

vital signs monitoring [9, 47, 55], machine vibration monitoring [18, 20], etc. For example, DoppleSleep [36] tracks sleep-related motions and classifies the sleep states using doppler radar. V<sup>2</sup>iFi [63] and Deepbreath [55] demonstrate multi-person respiration monitoring using UWB pulse radar and FMCW radar, respectively. However, these dedicated radar devices are usually specially deployed for sensing applications and their communication functionality is seldomly discussed.

**7.2.2 Sub-6G Communication Device-based Sensing.** Wi-Fi-based motion sensing has been explored in recent studies. The Wi-Fi channel state information (CSI) is obtained from different subcarriers. CSI can describe the propagation channel properties between the associated transmitter and receiver. For example, Gao et al. [14] proposed a position-independent gesture recognition by extracting moving features from the hand-oriented view. MultiSense [56] also demonstrates multi-person respiration monitoring by separating linear superimposed respiration using ICA. Recently, LoRa signals are also exploited for long-range indoor respiration monitoring [52, 57, 58]. Zhang et al. [58] performed beamforming on the LoRa gateway to achieve long-range multi-person respiration monitoring. Xie and Xiong [52] proposed the virtual fence to mitigate interference in the multi-person scenario. However, these sub-6GHz communication devices have limited bandwidth and antenna apertures, resulting in coarse range and angle resolution.

## 8 DISCUSSION

**Bi-directional simultaneous sensing and communication.** To extend to bi-directional simultaneous sensing and communication, here we discuss the uplink design. The client can perform concurrent uplink communication and sensing using *Sidense* architecture if it supports full-duplex. But if the AP needs to perform environment sensing during uplink communication, the scenario can be further divided into two cases:

- (1) Scenario 1: The sensing target is the transmitting client. In this case, the target (client) is located at the AP RX main lobe.
- (2) Scenario 2: The sensing target is not the transmitting client but a nearby object/person. Since the target is not the transmitting client (device-free sensing), the target is located at the AP RX sidelobe. To make things simple, we assume that the transmitting client is static.

Followings are the challenges in uplink sensing. The first challenge is present in both scenarios, while the second challenge is present only in Scenario 2. Here we also discuss the potential solutions:

- (1) Asynchronous clocks between the transmitter and receiver: Since the clock of the AP and client are not synchronized, the clock drift and frequency offset will directly lead to Doppler and range ambiguity [32]. Cross-antenna cross-correlation (CACC) is widely used in Wi-Fi sensing to remove the frequency offset [25, 35]. If the AP RX supports for MIMO, CACC can also be used to compensate for the frequency offset in uplink sensing, by calculating the correlation between signals from different antennas.
- (2) Limited angular sensing range: Similar to downlink sensing, due to the mmWave directional communication, the uplink sensing scope is limited to the communication direction. When AP is sensing during the uplink communication, it can adopt multibeam optimization to form a communication beam towards the client and a sensing beam towards the target. The sensing beam can enlarge the sensing range. Different from downlink sensing, the RX multibeam strategy will not decrease the transmission power nor cause extra interference.

**Target motion speed:** The time-domain integration module increases the received signal quality by accumulating packets, which will reduce the original sampling rate and limit the resolution of speed estimation. In 802.11ad, the DMG inter-packet interval is microsecond-level and can provide packet rates at tens of kHz [10]. As many indoor wireless sensing applications require a sampling rate that less than 1kHz [14, 49, 56, 58], *Sidense* can meet the sample rate requirement even after integration.

**Target Number Estimation.** The ICA algorithm requires the number of signal sources as an input. As the number of moving targets is unknown, we set the source number as the number of candidate sectors or observations. However, the candidate sectors derived from the target detection process may contain strong multipath signals (i.e., ghosts). This will result in the consequence that the number of candidate sectors is larger than the number of actual targets. There are some existing works that can separate targets and ghosts [15, 43]. *Sidense* can incorporate these methods to get a more accurate estimation of source number for the ICA process. We will leave this to our future work.

**Full bandwidth compatibility:** Due to the limitation of USRP bandwidth, in this paper, the signal bandwidth is limited to 100MHz. The purpose of the system evaluation is to validate the feasibility of side lobe sensing and results show that *Sidense* can achieve robust sensing performance. It is our future work to extend the bandwidth to 2GHz and generate 802.11 ad/ay compliant signals. We note that with a larger bandwidth, not only will the throughput increase, but also the sensing resolution. It is beneficial to both sensing and communication. Here we discuss two aspects of design that need to be considered when implementing full-band *Sidense*:

- (1) Beam switching control: The larger bandwidth means shorter packet duration, so the ultra-fast beam switch ability is important in full-band *Sidense* implementation. In this narrow band prototype, the beam switching is controlled by GPIO triggers. Since the GPIO commands come from the controller, it will cause a beam switching delay (about 0.7 ~ 1.5ms). Actually, the antenna RF settling time takes at most 35ns, and existing work has verified that ultrafast beam switching can be achieved by directly controlling the antenna through FPGA. Our future work will utilize the FPGA on a full-band platform for beam sweeping control to achieve ultra-fast beam switching.
- (2) Compensation for coherent integration: Coherent integration is widely used in modern wideband radar [54]. Similar to the monostatic radar, *Sidense* is full-duplex with synchronized TX/RX chains. As the bandwidth increases, the range resolution is improved. However, fast target motion in the coherent processing interval (CPI) will lead to the across range unit (ARU) effect and doppler frequency migration (DFM) in the wideband case [40, 44, 53]. So the length of CPI is limited by the target velocity and needs compensation for longer integration. Fortunately, existing research has proposed various time-frequency transform methods to achieve a long-time coherent integration process [8, 19, 40, 44, 53]. We may integrate these methods with *Sidense* to improve the performance of wideband integration.

**Hardware dependency:** The unique hardware requirements for implementation of *Sidense* are mainly in the target detection and preprocessing steps. It requires the system to meet the following requirements: full-duplex, TX/RX chain synchronization support, rapid beam sweeping capability, reconfigurable antenna weight codebook, and access to physical layer information. These hardware requirements are not harsh for existing equipment, and we believe that *Sidense* can be flexibly extended to other mmWave platforms. For instance, mm-FLEX [23] can provide ultra-fast antenna beam control and full-duplex capabilities. Besides, the current 60GHz commercial equipment supports multi-antenna synchronization and radar mode [50]. If the access to the physical layer information is allowed on these commercial devices [42], *Sidense* architecture can also be implemented on commercial mmWave devices for simultaneous directional communication and omni-directional sensing.

## 9 CONCLUSION

We present *Sidense*, a mmWave platform that supports simultaneous directional communication and quasi-omnidirectional sensing. *Sidense* does not require any modification to the communication process or the beam-forming strategy, and thus will not degrade the communication performance. Different from existing works, *Sidense* exploits the side-lobe energy in the antenna radiation pattern for sensing. As the side-lobe energy is weak and uneven, we design the time-domain integration and multi-target separation schemes to address the challenges in side-lobe sensing. Results show that *Sidense* can achieve 95<sup>th</sup> percentile displacement error of 5.79mm when

the device-to-target distance is 6m. We also demonstrate a case study for multi-person respiration monitoring, and the median error is 0BPM-1.2BPM at 2.3m, which is comparable to existing works. We believe that more fascinating applications can be implemented on the proposed joint sensing and communication platform.

## ACKNOWLEDGMENTS

We are truly grateful to all the anonymous reviewers for their insightful comments. This research is supported in part by the Key-Area Research and Development Program of Guangdong Province (No. 2020B010164001), in part by the National Natural Science Foundation of China (No. 62002150), in part by RGC (under Contract CERG 16203719, Contract 16204820, and Contract R8015), in part by the Major Key Project of PCL (No. PCL2021A15), and in part by Shenzhen Science, Technology and Innovation Commission Basic Research Project (No. JCYJ20180507181527806). Q. Huang and J. Zhang are the corresponding authors.

## REFERENCES

- [1] V. David Sánchez A. 2002. Frontiers of research in BSS/ICA. *Neurocomputing* 49, 1-4 (2002), 7–23. [https://doi.org/10.1016/S0925-2312\(02\)00533-7](https://doi.org/10.1016/S0925-2312(02)00533-7)
- [2] Fadel Adib, Zachary Kabelac, and Dina Katabi. 2015. Multi-Person Localization via RF Body Reflections. In *12th USENIX Symposium on Networked Systems Design and Implementation, NSDI 15, Oakland, CA, USA, May 4-6, 2015*. USENIX Association, 279–292. <https://www.usenix.org/conference/nsdi15/technical-sessions/presentation/adib>
- [3] Carlos Baquero Barneto, Sahan Damith Liyanaarachchi, Taneli Riihonen, Lauri Anttila, and Mikko Valkama. 2020. Multibeam design for joint communication and sensing in 5G New Radio networks. In *ICC 2020-2020 IEEE International Conference on Communications (ICC)*. IEEE, 1–6.
- [4] Carlos Baquero Barneto, Sahan Damith Liyanaarachchi, Taneli Riihonen, Mikko Heino, Lauri Anttila, and Mikko Valkama. 2020. Beamforming and Waveform Optimization for OFDM-based Joint Communications and Sensing at mm-Waves. In *54th Asilomar Conference on Signals, Systems, and Computers, ACSSC 2020, Pacific Grove, CA, USA, November 1-4, 2020*, Michael B. Matthews (Ed.). IEEE, 895–899. <https://doi.org/10.1109/IEEECONF51394.2020.9443340>
- [5] Carlos Baquero Barneto, Elizaveta Rastorgueva-Foi, Furkan Keskin, Taneli Riihonen, Matias Turunen, Jukka Talvitie, Henk Wymeersch, and Mikko Valkama. 2022. Millimeter-wave mobile sensing and environment mapping: Models, algorithms and validation. *IEEE Transactions on Vehicular Technology* (2022).
- [6] Carlos Baquero Barneto, Taneli Riihonen, Sahan Damith Liyanaarachchi, Mikko Heino, Nuria González-Prelcic, and Mikko Valkama. 2021. Beamformer design and optimization for full-duplex joint communication and sensing at mm-waves. *arXiv preprint arXiv:2109.05932* (2021).
- [7] Jean-François Cardoso and Antoine Souloumiac. 1993. Blind beamforming for non-Gaussian signals. In *IEE proceedings F (radar and signal processing)*, Vol. 140. IET, 362–370.
- [8] Xiaolong Chen, Jian Guan, Yong Huang, Ningbo Liu, and You He. 2015. Radon-Linear Canonical Ambiguity Function-Based Detection and Estimation Method for Marine Target With Micromotion. *IEEE Transactions on Geoscience and Remote Sensing* 53, 4 (2015), 2225–2240. <https://doi.org/10.1109/TGRS.2014.2358456>
- [9] Zhe Chen, Tianyue Zheng, Chao Cai, and Jun Luo. 2021. *MoVi-Fi*. Vol. 1. Association for Computing Machinery. 392–405 pages. 10.1145/3447993.3483251.
- [10] IEEE Computer Society LAN/MAN Standards Committee et al. 2012. *IEEE Standard for Information technology–Telecommunications and information exchange between systems–Local and metropolitan area networks–Specific requirements–Part 11: Wireless LAN Medium Access Control (MAC) and Physical Layer (PHY) Specifications Amendment 3: Enhancements for Very High Throughput in the 60 GHz Band*. <https://standards.ieee.org/ieee/802.11ad/4527/>
- [11] IEEE Computer Society LAN/MAN Standards Committee et al. 2021. *IEEE Standard for Information Technology–Telecommunications and Information Exchange between Systems Local and Metropolitan Area Networks–Specific Requirements Part 11: Wireless LAN Medium Access Control (MAC) and Physical Layer (PHY) Specifications Amendment 2: Enhanced Throughput for Operation in License-exempt Bands above 45 GHz*. <https://standards.ieee.org/ieee/802.11ay/6142/>
- [12] Demond Cureton. 2021. *VR, AR Firms To Ride Qualcomm mmWave*. <https://www.xrtoday.com/mixed-reality/vr-ar-firms-to-ride-qualcomm-mmwave/>
- [13] Martin Ester, Hans-Peter Kriegel, Jörg Sander, and Xiaowei Xu. 1996. A Density-Based Algorithm for Discovering Clusters in Large Spatial Databases with Noise. In *Proceedings of the Second International Conference on Knowledge Discovery and Data Mining (KDD-96), Portland, Oregon, USA*, Evangelos Simoudis, Jiawei Han, and Usama M. Fayyad (Eds.). AAAI Press, 226–231.

- [14] Ruiyang Gao, Mi Zhang, Jie Zhang, Yang Li, Enze Yi, Dan Wu, Leye Wang, and Daqing Zhang. 2021. Towards Position-Independent Sensing for Gesture Recognition with Wi-Fi. *Proc. ACM Interact. Mob. Wearable Ubiquitous Technol.* 5, 2 (2021), 61:1–61:28. <https://doi.org/10.1145/3463504>
- [15] Gianluca Gennarelli, Gemine Vivone, Paolo Braca, Francesco Soldovieri, and Moeness G Amin. 2016. Comparative analysis of two approaches for multipath ghost suppression in radar imaging. *IEEE Geoscience and Remote Sensing Letters* 13, 9 (2016), 1226–1230.
- [16] Emanuele Grossi, Marco Lops, Antonia Maria Tulino, and Luca Venturino. 2021. Opportunistic Sensing Using mmWave Communication Signals: A Subspace Approach. *IEEE Trans. Wirel. Commun.* 20, 7 (2021), 4420–4434. <https://doi.org/10.1109/TWC.2021.3058775>
- [17] Emanuele Grossi, Marco Lops, and Luca Venturino. 2020. Adaptive Detection and Localization Exploiting the IEEE 802.11ad Standard. *IEEE Trans. Wirel. Commun.* 19, 7 (2020), 4394–4407. <https://doi.org/10.1109/TWC.2020.2983032>
- [18] Junchen Guo, Meng Jin, Yuan He, Weiguo Wang, and Yunhao Liu. 2021. Dancing Waltz with Ghosts: Measuring Sub-mm-Level 2D Rotor Orbit with a Single mmWave Radar. In *IPSN '21: The 20th International Conference on Information Processing in Sensor Networks, Nashville, TN, USA, May, 2021*. ACM, 77–92.
- [19] Penghui Huang, Guisheng Liao, Zhiwei Yang, Xiang-Gen Xia, Jing-Tao Ma, and Jingting Ma. 2016. Long-Time Coherent Integration for Weak Maneuvering Target Detection and High-Order Motion Parameter Estimation Based on Keystone Transform. *IEEE Transactions on Signal Processing* 64, 15 (2016), 4013–4026. <https://doi.org/10.1109/TSP.2016.2558161>
- [20] Chengkun Jiang, Junchen Guo, Yuan He, Meng Jin, Shuai Li, and Yunhao Liu. 2020. mmVib: micrometer-level vibration measurement with mmwave radar. In *MobiCom '20: The 26th Annual International Conference on Mobile Computing and Networking, London, United Kingdom, September 21-25, 2020*. ACM, 45:1–45:13.
- [21] Preeti Kumari, Junil Choi, Nuria Gonzalez-Prelcic, and Robert W. Heath. 2018. IEEE 802.11ad-Based Radar: An Approach to Joint Vehicular Communication-Radar System. *IEEE Transactions on Vehicular Technology* 67, 4 (2018), 3012–3027. arXiv:1702.05833 10.1109/TVT.2017.2774762.
- [22] Preeti Kumari, Nuria González Prelcic, and Robert W. Heath Jr. 2015. Investigating the IEEE 802.11ad Standard for Millimeter Wave Automotive Radar. In *IEEE 82nd Vehicular Technology Conference, VTC Fall 2015, Boston, MA, USA, September 6-9, 2015*. IEEE, 1–5.
- [23] Jesus Omar Lacruz, Dolores Garcia, Pablo Jiménez Mateo, Joan Palacios, and Joerg Widmer. 2020. Mm-FLEX: An Open Platform for Millimeter-Wave Mobile Full-Bandwidth Experimentation. In *Proceedings of the 18th International Conference on Mobile Systems, Applications, and Services (Toronto, Ontario, Canada) (MobiSys '20)*. Association for Computing Machinery, New York, NY, USA, 1–13.
- [24] Shengjie Li, Zhaopeng Liu, Yue Zhang, Qin Lv, Xiaopeng Niu, Leye Wang, and Daqing Zhang. 2020. WiBorder: precise Wi-Fi based boundary sensing via through-wall discrimination. *Proceedings of the ACM on Interactive, Mobile, Wearable and Ubiquitous Technologies* 4, 3 (2020), 1–30.
- [25] Xiang Li, Daqing Zhang, Qin Lv, Jie Xiong, Shengjie Li, Yue Zhang, and Hong Mei. 2017. IndoTrack: Device-Free Indoor Human Tracking with Commodity Wi-Fi. *Proc. ACM Interact. Mob. Wearable Ubiquitous Technol.* 1, 3, Article 72 (sep 2017), 22 pages.
- [26] Jaime Lien, Nicholas Gillian, M. Emre Karagozler, Patrick Amihood, and Ivan Poupyrev. 2016. Soli: Ubiquitous Gesture Sensing with Millimeter Wave Radar. *Acm Transactions on Graphics* 35, 4 (2016), 1–19.
- [27] Chris Xiaoxuan Lu, Stefano Rosa, Peijun Zhao, Bing Wang, Changhao Chen, John A. Stankovic, Niki Trigoni, and Andrew Markham. 2020. See through smoke: robust indoor mapping with low-cost mmWave radar. In *MobiSys '20: The 18th Annual International Conference on Mobile Systems, Applications, and Services, Toronto, Ontario, Canada, June 15-19, 2020*, Eyal de Lara, Iqbal Mohamed, Jason Nieh, and Elizabeth M. Belding (Eds.). ACM, 14–27.
- [28] L A N Man, Standards Committee, and Ieee Computer. 2012. *Part 11 : Wireless LAN Medium Access Control ( MAC ) and Physical Layer ( PHY ) Specifications Amendment 3 : Enhancements for Very High Throughput in the 60 GHz Band IEEE Computer Society*. Vol. 2012.
- [29] Dolores García Martí, Jesus Omar Lacruz, Pablo Jiménez Mateo, and Joerg Widmer. 2020. POLAR: Passive object localization with IEEE 802.11ad using phased antenna arrays. In *39th IEEE Conference on Computer Communications, INFOCOM 2020, Toronto, ON, Canada, July 6-9, 2020*. IEEE, 1838–1847. <https://doi.org/10.1109/INFOCOM41043.2020.9155383>
- [30] The MathWorks. 2021. 802.11ad Packet Error Rate Single Carrier PHY Simulation with TGay Channel. <https://www.mathworks.com/help/wlan/ug/802-11ad-packet-error-rate-single-carrier-phy-simulation-with-tgay-channel.html>
- [31] JP McFadden, RC Price, HD Eastwood, and RS Briggs. 1982. Raised respiratory rate in elderly patients: a valuable physical sign. *Br Med J (Clin Res Ed)* 284, 6316 (1982), 626–627.
- [32] Zhitong Ni, J Andrew Zhang, Xiaojing Huang, Kai Yang, and Jinhong Yuan. 2021. Uplink sensing in perceptive mobile networks with asynchronous transceivers. *IEEE Transactions on Signal Processing* 69 (2021), 1287–1300.
- [33] Jacopo Pegoraro, Jesus Omar Lacruz, Enver Bashirov, Michele Rossi, and Joerg Widmer. 2021. RAPID: Retrofitting IEEE 802.11 ay Access Points for Indoor Human Detection and Sensing. *arXiv preprint arXiv:2109.04819* (2021).
- [34] Lorenzo Pucci, Enrico Paolini, and Andrea Giorgetti. 2022. System-Level Analysis of Joint Sensing and Communication based on 5G New Radio. *IEEE Journal on Selected Areas in Communications (Early Access)* (2022), 1–12.
- [35] Kun Qian, Chenshu Wu, Yi Zhang, Guidong Zhang, Zheng Yang, and Yunhao Liu. 2018. Widar2.0: Passive Human Tracking with a Single Wi-Fi Link. In *Proceedings of the 16th Annual International Conference on Mobile Systems, Applications, and Services, MobiSys 2018, Munich, Germany, June 10-15, 2018*, Jörg Ott, Falko Dressler, Stefan Saroiu, and Prabal Dutta (Eds.). ACM, 350–361.

- [36] Tauhidur Rahman, Alexander Travis Adams, Ruth Vinisha Ravichandran, Mi Zhang, Shwetak N. Patel, Julie A. Kientz, and Tanzeem Choudhury. 2015. Dopplesleep: a contactless unobtrusive sleep sensing system using short-range Doppler radar. In *Proceedings of the 2015 ACM International Joint Conference on Pervasive and Ubiquitous Computing, UbiComp 2015, Osaka, Japan, September 7-11, 2015*, Kenji Mase, Marc Langheinrich, Daniel Gatica-Perez, Hans Gellersen, Tanzeem Choudhury, and Koji Yatani (Eds.). ACM, 39–50.
- [37] Sai Deepika Regani, Chenshu Wu, Beibei Wang, Min Wu, and KJ Ray Liu. 2021. mmWrite: passive handwriting tracking using a single millimeter-wave radio. *IEEE Internet of Things Journal* 8, 17 (2021), 13291–13305.
- [38] Mark A Richards. 2014. *Fundamentals of radar signal processing*. McGraw-Hill Education.
- [39] Panneer Selvam Santhalingam, Al Amin Hosain, Ding Zhang, Parth H. Pathak, Huzefa Rangwala, and Raja S. Kushalnagar. 2020. mmASL: Environment-Independent ASL Gesture Recognition Using 60 GHz Millimeter-wave Signals. *Proc. ACM Interact. Mob. Wearable Ubiquitous Technol.* 4, 1 (2020), 26:1–26:30.
- [40] Shijian Shen, Xin Nie, Lan Tang, Yechao Bai, Xinggan Zhang, Lei Li, and De Ben. 2020. An improved coherent integration method for wideband radar based on two-dimensional frequency correction. *Electronics* 9, 5 (2020), 840.
- [41] Sivers-Semiconductors. 2021. *RF Modules*. <https://www.sivers-semiconductors.com/rf-modules/>
- [42] Daniel Steinmetzer, Daniel Wegemer, Matthias Schulz, Joerg Widmer, and Matthias Hollick. 2017. Compressive Millimeter-Wave Sector Selection in Off-the-Shelf IEEE 802.11ad Devices. In *Proceedings of the 13th International Conference on Emerging Networking EXperiments and Technologies* (Incheon, Republic of Korea) (CoNEXT '17). Association for Computing Machinery, New York, NY, USA, 414–425.
- [43] Qinyan Tan, Henry Leung, Yaoliang Song, and Towe Wang. 2014. Multipath ghost suppression for through-the-wall radar. *IEEE Trans. Aerospace Electron. Systems* 50, 3 (2014), 2284–2292.
- [44] Ran Tao, Ning Zhang, and Yunchu Wang. 2011. Analysing and compensating the effects of range and Doppler frequency migrations in linear frequency modulation pulse compression radar. *IET radar, sonar & navigation* 5, 1 (2011), 12–22.
- [45] Vutha Va and Robert W. Heath Jr. 2016. Performance Analysis of Beam Sweeping in Millimeter Wave Assuming Noise and Imperfect Antenna Patterns. In *IEEE 84th Vehicular Technology Conference, VTC Fall 2016, Montreal, QC, Canada, September 18-21, 2016*. IEEE, 1–5. <https://doi.org/10.1109/VTCFall.2016.7881150>
- [46] Vernier. 2021. *Go Direct Respiration Belt*. <https://www.vernier.com/product/go-direct-respiration-belt/>
- [47] Fengyu Wang, Xiaolu Zeng, Chenshu Wu, Beibei Wang, and K. J. Ray Liu. 2021. MmHRV: Contactless Heart Rate Variability Monitoring Using Millimeter-Wave Radio. *IEEE Internet of Things Journal* 8, 22 (2021), 16623–16636. 10.1109/JIOT.2021.3075167.
- [48] Fengyu Wang, Feng Zhang, Chenshu Wu, Beibei Wang, and K. J. Ray Liu. 2021. ViMo: Multiperson Vital Sign Monitoring Using Commodity Millimeter-Wave Radio. *IEEE Internet Things J.* 8, 3 (2021), 1294–1307.
- [49] Teng Wei and Xinyu Zhang. 2015. mTrack: High-Precision Passive Tracking Using Millimeter Wave Radios. In *Proceedings of the 21st Annual International Conference on Mobile Computing and Networking, MobiCom 2015, Paris, France, September 7-11, 2015*, Serge Fdida, Giovanni Pau, Sneha Kumar Kasera, and Heather Zheng (Eds.). ACM, 117–129.
- [50] Chenshu Wu, Feng Zhang, Beibei Wang, and K. J. Ray Liu. 2020. mmTrack: Passive Multi-Person Localization Using Commodity Millimeter Wave Radio. In *39th IEEE Conference on Computer Communications, INFOCOM 2020, Toronto, ON, Canada, July 6-9, 2020*. IEEE, 2400–2409.
- [51] Chenshu Wu, Feng Zhang, Beibei Wang, and KJ Ray Liu. 2020. mSense: Towards mobile material sensing with a single millimeter-wave radio. *Proceedings of the ACM on Interactive, Mobile, Wearable and Ubiquitous Technologies* 4, 3 (2020), 1–20.
- [52] Binbin Xie and Jie Xiong. 2020. Combating interference for long range LoRa sensing. *SenSys 2020 - Proceedings of the 2020 18th ACM Conference on Embedded Networked Sensor Systems* (2020), 69–81. 10.1145/3384419.3430731.
- [53] Jia Xu, Ji Yu, Ying-Ning Peng, and Xiang-Gen Xia. 2011. Radon-Fourier transform for radar target detection, I: generalized Doppler filter bank. *IEEE transactions on aerospace and electronic systems* 47, 2 (2011), 1186–1202.
- [54] J Xu, J Yu, Y-N Peng, X-G Xia, and T Long. 2012. Space-time Radon-Fourier transform and applications in radar target detection. *IET Radar, Sonar & Navigation* 6, 9 (2012), 846–857.
- [55] Shichao Yue, Hao He, Hao Wang, Hariharan Rahul, and Dina Katabi. 2018. Extracting Multi-Person Respiration from Entangled RF Signals. *Proceedings of the ACM on Interactive, Mobile, Wearable and Ubiquitous Technologies* 2, 2 (2018), 1–22. 10.1145/3214289.
- [56] Youwei Zeng, Dan Wu, Jie Xiong, Jinyi Liu, Zhaopeng Liu, and Daqing Zhang. 2020. MultiSense: Enabling multi-person respiration sensing with commodity wifi. *Proceedings of the ACM on Interactive, Mobile, Wearable and Ubiquitous Technologies* 4, 3 (2020), 1–29.
- [57] Fusang Zhang, Zhaoxin Chang, Kai Niu, Jie Xiong, Beihong Jin, Qin Lv, and Daqing Zhang. 2020. Exploring lora for long-range through-wall sensing. *Proceedings of the ACM on Interactive, Mobile, Wearable and Ubiquitous Technologies* 4, 2 (2020), 1–27.
- [58] Fusang Zhang, Zhaoxin Chang, Jie Xiong, Rong Zheng, Junqi Ma, Kai Niu, Beihong Jin, and Daqing Zhang. 2021. Unlocking the Beamforming Potential of LoRa for Long-range Multi-target Respiration Sensing. *Proc. ACM Interact. Mob. Wearable Ubiquitous Technol.* 5, 2 (2021), 85:1–85:25.
- [59] Feng Zhang, Chenshu Wu, Beibei Wang, and KJ Ray Liu. 2020. mmEye: Super-resolution millimeter wave imaging. *IEEE Internet of Things Journal* 8, 8 (2020), 6995–7008.
- [60] J Andrew Zhang, Xiaojing Huang, Y Jay Guo, Jinhong Yuan, and Robert W Heath. 2018. Multibeam for joint communication and radar sensing using steerable analog antenna arrays. *IEEE Transactions on Vehicular Technology* 68, 1 (2018), 671–685.

- [61] Mingmin Zhao, Tianhong Li, Mohammad Abu Alsheikh, Yonglong Tian, Hang Zhao, Antonio Torralba, and Dina Katabi. 2018. Through-Wall Human Pose Estimation Using Radio Signals. In *2018 IEEE Conference on Computer Vision and Pattern Recognition, CVPR 2018, Salt Lake City, UT, USA, June 18-22, 2018*. Computer Vision Foundation / IEEE Computer Society, 7356–7365.
- [62] Mingmin Zhao, Yonglong Tian, Hang Zhao, Mohammad Abu Alsheikh, Tianhong Li, Rumen Hristov, Zachary Kabelac, Dina Katabi, and Antonio Torralba. 2018. RF-based 3D skeletons. In *Proceedings of the 2018 Conference of the ACM Special Interest Group on Data Communication, SIGCOMM 2018, Budapest, Hungary, August 20-25, 2018*, Sergey Gorinsky and János Tapolcai (Eds.). ACM, 267–281. <https://doi.org/10.1145/3230543.3230579>
- [63] Tianyue Zheng, Zhe Chen, Chao Cai, Jun Luo, and Xu Zhang. 2020. V2iFi: in-Vehicle Vital Sign Monitoring via Compact RF Sensing. *Proc. ACM Interact. Mob. Wearable Ubiquitous Technol.* 4, 2 (2020), 70:1–70:27. <https://doi.org/10.1145/3397321>